[American Journal of Science, Vol. 320, September, 2020, P. 599–636, DOI 10.2475/09.2020.02]

# SIMULATING METEORIC AND MIXING ZONE CARBONATE DIAGENESIS WITH A TWO-DIMENSIONAL REACTIVE TRANSPORT MODEL

MINGYU ZHAO*,†, NOAH PLANAVSKY*, AMANDA M. OEHLERT**, GUANGYI WEI*, and ZHENG GONG*

**ABSTRACT. Meteoric and mixing-zone diagenesis can dramatically alter the geochemical signatures of shallow marine carbonates. Most preserved pre-Cretaceous carbonates were deposited in shallow marine environments and thus may have been susceptible to meteoric and mixing-zone diagenesis. However, a quantitative understanding of how the geochemical composition of carbonates changes during diagenesis still requires further development. Here, we present a new two-dimensional (2D) reactive transport model coupled with a 2D coastal hydrology model to simulate carbonate diagenesis and provide insights into its impact on the isotopic and elemental compositions of carbonates in the geological record. Using this model, we have simulated the stratigraphic trends and relationship between isotopic records (for example, $\delta^{13}C$ and $\delta^{18}O$ values) observed in modern (Recent-Miocene) sections where the impact of meteoric diagenesis has been clearly characterized. Our model can also reproduce anomalous Neoproterozoic carbonate geochemical profiles where the effects of meteoric diagenesis have been debated. Further, our model indicates that linear carbonate C-O isotope co-variations can either be generated in the mixing zone between freshwater and marine pore waters, or in the freshwater phreatic zone with a downward decrease in recrystallization (with no net carbonate dissolution or precipitation) rate. In addition, numerous processes were observed to decouple $\delta^{18}O_{carb}$ values from other isotopic and elemental signatures during carbonate diagenesis, indicating that a lack of linear correlation between $\delta^{18}O_{carb}$ values and other geochemical variables does not necessarily suggest limited meteoric alteration. Sensitivity analyses show that the steady-state timescale is controlled by compositional differences between fluid endmembers, the calcite-water element distribution coefficient, the recrystallization rate, porosity, and the groundwater discharge rate. Given that reactive transport models have proven to be powerful theoretical tools in many disciplines of Earth sciences, our hope is that this model will promote a more quantitative understanding of meteoric and mixing zone diagenesis of marine carbonates.**

Key words: carbonate, meteoric diagenesis, model, carbon isotope, oxygen isotope, mixing zone

## INTRODUCTION

The ability to reconstruct ancient oceanic conditions through carbonate records largely hinges on understanding the extent to which the primary signal has been reset by carbonate diagenesis. Meteoric diagenesis in coastal aquifers is recognized as the most important process that may overprint the primary signal, as the geochemical composition of meteoric water is quite different from that of seawater. Carbonate alteration by meteoric water is typically linked to shifts in hydrology driven by sea level fluctuations (Land and Epstein, 1970; Allan and Matthews, 1982; James and Choquette 1984; Swart, 2015). There has been extensive work documenting the effects of meteoric and mixing-zone alteration, and numerous authors have proposed that this process has a major impact on the carbonate record (Swart, 2015 and references therein). Sustained work on diagenesis in modern carbonate platforms over the past few decades has dramatically improved our understanding of these processes (for

* Department of Geology and Geophysics, Yale University, Connecticut, USA
** Rosenstiel School of Marine and Atmospheric Sciences, University of Miami, Florida, USA
† Corresponding author: mingyu.zhao@yale.edu

example, Clayton and Degens, 1959; Gross, 1964; Land and Epstein, 1970; Allan and Matthews, 1982; Budd, 1988; Sanford and Konikow, 1989; McClain and others, 1992; Swart, 2000; Melim and others, 2002, 2004; Whitaker and Smart, 2007; Swart, 2008; Swart and Kennedy, 2012; Oehlert and Swart, 2014; Swart and Oehlert, 2018).

Water-rock interaction models have long been used to explore meteoric carbonate diagenesis (for example, Land, 1980; Meyers, 1989; Banner and Hanson, 1990; Jacobsen and Kaufman, 1999; Derry, 2010). However, water-rock interaction models do not describe the evolution and transport of fluids across space as a driver for the kinetics of recrystallization processes (see Steefel and Maher, 2009 for discussion of the importance of transport on reactions). Given that the alteration of nearshore carbonates is dynamic with variable-density flow (Sanford and Konikow, 1989; Rezaei and others, 2005) and perhaps varying recrystallization rates across space (for example, Swart and Oehlert, 2018), there is a motivation to explore diagenetic models that are able to capture heterogeneous fluids and carbonate system evolution towards steady state. Further, there are variations in flow direction within coastal aquifers, so a model with at least two dimensions is required to describe the hydrology and geochemical variations.

Another complexity in modeling carbonate alteration is that porewaters in the mixing zone are a continuous mixture of seawater and groundwater/freshwater generated by hydrodynamic dispersion (Bear and Verruijt, 2012). Water-rock interaction models are able to simulate the interaction between carbonate sediments and a single fluid, such as freshwater. For interactions between carbonate sediments and seawater-freshwater mixtures, it has been suggested that the geochemical compositions of the resulting diagenetic carbonate will lie between the water-rock interaction and seawater-freshwater mixing curves (Banner and Hanson, 1990). However, a direct simulation of the time-dependent variations in carbonate composition during the interaction between carbonates and a continuous spectrum of seawater-freshwater mixtures hasn't yet been performed. It has been suggested that the classic positive correlation between C and O isotopic values forms in the mixing zone (Allan and Matthews, 1982; Melim and others, 2002, 2004; Swart and Kennedy, 2012; Zhao and Zheng, 2017), with a gradual decrease in both C and O isotopic values upsection. It has also been hypothesized that this positive correlation may instead be generated in the freshwater phreatic zone by varying recrystallization rates (Swart and Oehlert, 2018). Thus, a model that captures the spatiotemporal complexity of diagenetic processes in the meteoric and mixing zones is necessary to understand the mechanisms that generate positive covariation between carbon and oxygen isotope values. Furthermore, this model should be able to describe the variations in the geochemical compositions of carbonates that result from their interaction with a spectrum of seawater-freshwater mixtures.

Hydrological and reactive transport models have been extensively used to simulate groundwater circulation, carbonate dissolution, dolomitization, porosity evolution, and residence times in the diagenetic zones of carbonate aquifers (Sanford and Konikow, 1989; Whitaker and Smart, 1990; Kaufman, 1994; Jones and others, 2004; Jones and Xiao, 2005; Rezaei and others, 2005; Paterson and others, 2008), as coastal hydrology (that is, the transport process) is one of the most critical driving forces of carbonate diagenesis. Reactive transport models have also been used to track the sources and sinks of elemental and isotopic compositions, elemental distribution coefficients, isotopic fractionation factors, and recrystallization rates of carbonates during marine burial diagenesis (Fantle and DePaolo, 2006, 2007; Higgins and Schrag, 2010, 2012; Fantle and Higgins, 2014; Fantle, 2015). However, the use of hydrological and reactive transport models to explore geochemical variations during meteoric and mixing zone diagenesis of carbonates is limited. Recently, 1D and 2D reactive transport

models have been used to simulate the variation of C and O isotopes during meteoric diagenesis (Dyer and others, 2017; Ahm and others, 2018). However, as these models only include a single initial fluid endmember, further development is required to simulate diagenesis in the mixing zone, where the diagenetic fluid is a continuous mixture of meteoric water and marine pore water. Addressing the complexities of carbonate diagenesis in coastal aquifers requires a 2D reactive transport model coupled with a hydrological model that describes the variable-density flow.

We employ a 2D variable-density hydrological model to calculate the direction and rates of water flow and then apply this flow information to a multi-component, time-dependent, 2D reactive transport model in order to investigate the kinetics of elemental and isotopic alteration during meteoric diagenesis. This model can capture the spatiotemporal variations of fluid and its reactions with carbonate minerals and, as a result, is well-suited to exploring the effects of low temperature diagenesis in shallow marine carbonates. In comparison with the previous models (Banner and Hanson, 1990; Jacobsen and Kaufman, 1999; Derry, 2010; Dyer and others, 2017; Ahm and others, 2018), our model can directly simulate the interaction between carbonate sediments and a continuous spectrum of seawater-freshwater mixtures in the mixing zone, which makes it possible to calculate the spatiotemporal variations of carbonate compositions during meteoric and mixing-zone diagenesis. Although some simplifications are necessary in all modeling approaches (that is here, sediment advection and various biogeochemical reactions, for example, have yet to be incorporated), our new model improves on the complexity and quantitative assessment of spatiotemporal heterogeneity of the coastal marine diagenetic environments. This model provides a new framework to quantitatively understand diagenetic processes occurring on carbonate platforms when they are exposed to meteoric waters.

## METHODS

### *Modeling Freshwater Incursions*

Freshwater incursions into marine sediments are primarily driven by periods of subaerial exposure. In the recent geological past, glacial-interglacial cycles have promoted periodic subaerial exposure of shallow marine carbonates and have established a predictable suite of diagenetic zones (for example, Allan and Matthews, 1982; Paterson and others, 2008; Swart and Oehlert, 2018). These orbitally driven sea level oscillations have the potential to repeatedly change the chemistry of the porewaters and overall fluid-rock interaction time within each diagenetic zone through time (Paterson and others, 2008). While parameterization of the processes and rates remains poorly constrained, some have suggested that residence times within a diagenetic zone may be largely unaffected during small amplitude sea level fluctuations (Paterson and others, 2008), and that the most significant alteration of $\delta^{13}C$ and $\delta^{18}O$ values may occur during the first period of subaerial exposure (Melim and others, 2004; Swart and Oehlert, 2018). Therefore, although we recognize that repeated freshwater incursions are a common phenomenon in the geological record, we focus on the effects of a single freshwater incursion in this study. Furthermore, we propose that the predicted timescales for alteration, which we show will vary with changing recrystallization rate, could be interpreted as cumulative reaction times during multiple subaerial exposure events.

### *Model Description*

We use the software package SUTRA to simulate 2D transient saturated variable-density flow in a coastal aquifer. The flow is calculated using Darcy's Law:

$$v = -\left(\frac{k}{\phi\mu}\right) \cdot (\nabla p - \rho g) \tag{1}$$

Where $k$ is solid matrix permeability, $\phi$ is the porosity of the unconsolidated carbonate sediments, $\mu$ is fluid viscosity, $p$ is fluid pressure, $\rho$ is fluid density and $g$ is gravitational acceleration. The fluid mass balance and solute (salt) mass balance are governed by the following equations, respectively (Voss and Provost, 2010):

$$(\rho S_{op})\frac{\partial p}{\partial t} + \left(\phi\frac{\partial \rho}{\partial C}\right)\frac{\partial C}{\partial t} - \nabla \cdot \left[\left(\frac{k\rho}{\mu}\right) \cdot (\nabla p - \rho g)\right] = Q_p \tag{2}$$

$$\frac{\partial(\phi\rho C)}{\partial t} = -\nabla \cdot (\phi\rho \mathrm{v} C) + \nabla\cdot[\phi\rho(D_m I + D) \cdot \nabla C] + Q_p C* \tag{3}$$

Where $\rho = \rho_0 + \frac{\partial \rho}{\partial C}C$ and $S_{op} = (1-\phi) * \alpha + \phi * \beta$, $S_{op}$ is specific pressure storativity, $t$ is time, $C$ is solute (salt in this study) mass fraction in fluid, $Q_p$ is fluid mass source (water mass plus solute mass), $\rho_0$ is the fluid density of pure water, $\partial\rho/\partial C$ is a constant value of density change with concentration, $\alpha$ is porous matrix compressibility, $\beta$ is fluid compressibility, $D_m$ is the molecular diffusion, $D$ is the mechanical dispersion, $I$ is the identity tensor matrix (1 on the diagonal, 0 elsewhere) and $C^*$ is the solute concentration in fluid sources. Using the calculated flows from the SUTRA run as an input data, we then applied a 2D reactive transport model to describe the geochemical changes in both carbonates and fluids during the meteoric and mixing-zone diagenesis:

$$\frac{\partial C_s}{\partial t} = -R(C_s - C_{eq}) \tag{4}$$

$$\frac{\partial C_l}{\partial t} = \frac{1}{\phi}\nabla \cdot (\phi(D_m I + D) \cdot \nabla C_l) - \frac{1}{\phi}\nabla \cdot (\phi \mathrm{v} C_l) + RF(C_s - C_{eq}) \tag{5}$$

where $R$ ($\mathrm{yr}^{-1}$) is the recrystallization rate of carbonates. $C_s$ and $C_l$ are the concentrations of a specific component (for example, C, O, $^{13}$C and $^{18}$O) of the carbonate sediment and fluid, respectively. $C_{eq}$ is the concentration of a specific carbonate component in equilibrium with fluids. $F = (1 - \phi)/\phi$. As all the units of concentrations in both solids and solutes are in mmol/L in the model, the F term does not contain the density of solids. In this study, we lump the effect of mechanical dispersion and molecular diffusion into one term ($D_m$). The only reaction included here is recrystallization, so the porosity of the system does not evolve through time. The effects of compaction and sediment advection are not considered in this model. A static system without changes in hydrology or endmember compositions is assumed before steady state is reached for the geochemical compositions of carbonate (usually >2 Myr). For trace elements (Mn and Sr) and their isotopes, distribution coefficients are used to describe partitioning between calcite and fluids:

$$K_D = \frac{C_s/Ca_s}{C_l/Ca_l} \tag{6}$$

Where $Ca_s$ and $Ca_l$ represent calcium (Ca) concentrations in carbonates and fluids, respectively. If the abundance of the two modeled isotopes of an element (such as $^{12}$C and $^{13}$C, $^{16}$O and $^{18}$O) are > 99 percent of the modeled element, we overlook the other isotopes and treat the sum of these two isotopes as the concentration of the modeled element, which only has a minor effect on the final results. For strontium (Sr), the concentration is a sum of the concentrations of its four isotopes ($^{84}$Sr, $^{86}$Sr, $^{87}$Sr and $^{88}$Sr), with $^{84}$Sr/$^{86}$Sr = 0.0565 and $^{88}$Sr/$^{86}$Sr = 8.37521. These element

concentrations and the isotopes in the numerator (for example, Sr concentration and $^{87}Sr$) are modeled together to understand the variations of isotopic compositions during diagenesis.

We assume that alteration can be modeled as recrystallization, without net loss or gain of carbonate during the alteration, and thus the concentrations of Ca and dissolved inorganic carbon (DIC) in interacting fluids do not evolve through time. Thus, for elements C, O, or Ca:

$$C_{eq} = C_s \tag{7}$$

where $C_s$ represents the solid phase concentration for each element (C, O, or Ca). For the elements Mn or Sr:

$$C_{eq} = \mathrm{K}_D C_l \mathrm{Ca}_s / \mathrm{Ca}_l \tag{8}$$

where $C_l$ represents the concentration of Mn or Sr in fluids. For $^{13}C$ or $^{18}O$:

$$C_{eq} = C_s / (1 + 1 / (\alpha C_{il} / (C_l - C_{il}))) \tag{9}$$

where $C_{il}$ represents the concentration of the relevant isotope ($^{13}C$ or $^{18}O$) in fluid, $C_s$ and $C_l$ represent the corresponding element concentration (C or O) in the solid and fluid phases, respectively. $\alpha$ is the isotopic fractionation factor.

For $^{87}Sr$:

$$C_{eq} = \mathrm{K}_D C_l \mathrm{Ca}_s / \mathrm{Ca}_l / (1 + 1 / (\alpha C_{il} / (C_l - C_{il}))) \tag{10}$$

where $C_{il}$ represents the concentration of the isotope $^{87}Sr$ in fluid, $C_s$ and $C_l$ represent Sr concentration in the solid and fluid phases, respectively. Each component (for example, C, O, $^{13}C$ and $^{18}O$) can be calculated together or separately during a single run. To model the sedimentary profile, we take a vertical slice from the 2D results.

We follow a standard procedure to run SUTRA. First, a steady-state simulation calculates pressure in the model domain prior to seawater intrusion (when all water in the model domain is freshwater) (Voss and Provost, 2010), and then the calculated pressure is applied as the initial pressure condition for the transient simulation. The mesh and boundary conditions are shown in figure 1A. Freshwater/groundwater recharge was set along the left boundary, while hydrostatic seawater pressure was set at the right boundary. In this study, groundwater is synonymous with freshwater. Seawater intrusion is a result of seawater's higher density, relative to freshwater. There is no flux across the top and bottom boundaries. The mesh is made up of 100 by 40 elements, each 10m by 5m, for a final model domain of 1000m in width and 200m in height (fig. 1A). The total length scale and the resolution are similar to previous studies on calcite dissolution in the mixing zone (Sanford and Konikow, 1989; Rezaei and others, 2005). For the transient runs, the time step size is $6 \times 10^6$ s (~0.19 years). One thousand time-steps are used to achieve steady state for pressure, salinity, and flows. The direct solver is used for the pre-simulations and the transient runs.

The 2D reaction-transport model is made in R (R Development Core Team, 2006). The method of lines is used to solve the partial differential equations (PDEs). The central-difference method is used for the advection term during the transformation of PDEs to ordinary differential equations (ODEs). The generated ODEs are solved by the "lsodes" solver (Soetaert and others, 2010). We have compared the results of our model with a 1D benchmark using an analytical solution in order to see whether the numerical solution produced by our model is accurate (fig. A1). Our model results do not have visible differences ($R^2 = 0.99999$) when compared with the 1D analytical solution (fig. A1), suggesting that our method is accurate. For the 2D reaction-transport simulations, the flow field is derived from the results of the SUTRA runs. For

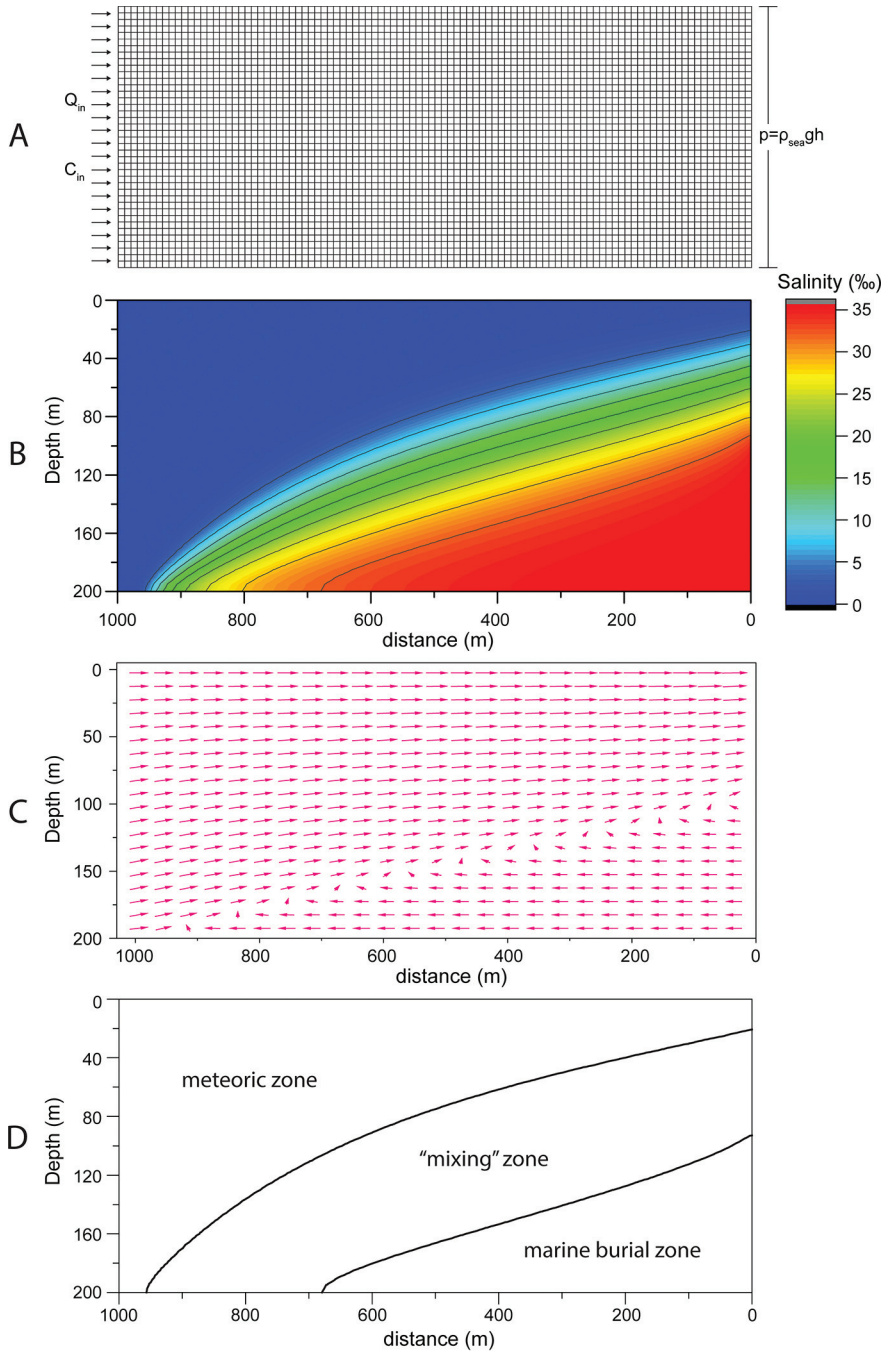


Fig. 1. Mesh, boundary conditions, salinity variations, flow directions and the division of diagenetic zones for the baseline run. (A) The 100×40 mesh and the boundary conditions of the model. (B) The distribution of salinity values for the steady state of the SUTRA run. The curves represent 10% to 90% seawater salinity. (C) The flow directions of the SUTRA run. Arrow lengths represent the logarithm of the flow rates in dm/yr. For clarity, only a portion of the data points are shown. (D) The division of diagenetic zones. The two curves represent 10% and 90% seawater salinity respectively. See table 1 for parameters of this baseline run.

TABLE 1

*Parameters for the baseline run of the hydrology model*

| parameters | description | values | units | references |
|---|---|---|---|---|
| $\phi$ | porosity | 0.35 | | Melim and others (2001) |
| B | aquifer thickness | 1 | m | |
| $C_{sea}$ | solute concentration of seawater | 0.0357 | $\frac{\text{kg (dissolved solids)}}{\text{kg(seawater)}}$ | Voss and Provost (2010) |
| $C_{IN}$ | solute concentration of freshwater | 0 | $\frac{\text{kg (dissolved solids)}}{\text{kg(seawater)}}$ | |
| $\rho_{sea}$ | density of seawater | 1024.99 | $kg/m^3$ | Voss and Provost (2010) |
| $\rho_o$ | density of freshwater | 1000 | $kg/m^3$ | |
| $\frac{\partial \rho}{\partial C}$ | a constant value for density change with concentration | 700 | $\frac{\text{kg(seawater)}}{\text{kg (dissolved solids)}\ m^3}$ | Voss and Provost (2010) |
| $\lvert g \rvert$ | gravitational acceleration | 9.8 | $m/s^2$ | |
| $Q_{IN}$ | total fluid mass source to each cell | $2.64*10^{-4}$ | $kg/(m^2 \cdot s)$ | Sanford and Konikow (1989) |
| $\alpha$ | porous matrix compressibility | $1.0*10^{-8}$ | $m \cdot s^2/kg$ | Voss and Provost (2010) |
| $\beta$ | fluid compressibility | $4.47*10^{-10}$ | $m \cdot s^2/kg$ | Voss and Provost (2010) |
| $\mu$ | fluid viscosity | $1.0*10^{-3}$ | $kg/m \cdot s$ | Voss and Provost (2010) |
| $k_H$ | horizontal solid matrix permeability | $1*10^{-11}$ | $m^2$ | Melim and others (2001); Jones and others (2004) |
| $k_V$ | vertical solid matrix permeability | $1*10^{-13}$ | $m^2$ | Melim and others (2001); Jones and others (2004) |
| $D_m$ | apparent molecular diffusivity (including tortuosity effects) | $1*10^{-6}$ | $m^2/s$ | |

fluids, freshwater composition is set at the left boundary and seawater composition is set for inflowing fluid at the right boundary. For each run, the initial conditions for carbonates and fluids are set as the elemental and isotopic composition of primary carbonate and seawater, respectively. Compositions of freshwater, seawater and unaltered carbonates used in the baseline run are shown in table 2. Time-dependent runs are executed to understand the variations of geochemical compositions at different degrees of alteration (DOA) during diagenesis. The DOA is the extent to which diagenesis has happened, or the extent to which the current carbonate composition ($C_s$) approaches the ultimate composition at steady state ($C_{ss}$). DOA is calculated by $DOA = (C_s\text{-}C_0)/(C_{ss}\text{-}C_0)$, where $C_0$ is the initial carbonate composition.

*Model Parametrization*

The hydrological parameters of the baseline run for the transient simulation are shown in table 1 and were selected to represent the typical conditions found in coastal carbonate aquifers. The porosity was set to 0.35, chosen as the median value from the shallow end (<1 km) of the coastal carbonate aquifer (Melim and others, 2001; Jones and others, 2004). For the baseline run, the horizontal and vertical permeability ($k_H$ and $k_V$) were set to $10^{-11}$ and $10^{-13}$ $m^2$ (table 1), respectively, within the typical range of permeability in carbonate platforms (Melim and others, 2001; Jones and others, 2004). The anisotropy of permeability ($k_H/k_V$) in carbonate platform is likely in the

TABLE 2

*Parameters for the baseline run of the reaction transport model*

| parameters | | values | units | references |
|---|---|---|---|---|
| $\rho$ | density of sediments | 2.6 | $g/cm^3$ | |
| R | recrystallization rate | $1*10^{-5}$ | $yr^{-1}$ | Allan and Matthews (1982) |
| $\delta^{13}C_{FW}$ | carbon isotope composition of groundwater | 0.3 | ‰ | |
| $DIC_{FW}$ | DIC concentration of groundwater | 1.2 | mM | Langmuir (1997) |
| $DIC_{SW}$ | DIC concentration of seawater | 2.3 | mM | Chester (2012) |
| $\delta^{13}C_{calci}$ | Carbon isotopic composition of unaltered calcite | 3.8 | ‰ | Oehlert and Swart (2014) |
| $\alpha^{13}C_{calc\text{-}W}$ | Carbon isotope fractionation factor between calcite and water | 0.9988 | | Hayes and others (1999) |
| $\delta^{18}O_{FW}$ | oxygen isotopic composition of groundwater | -2.5 | ‰ SMOW | Bowen and Revenaugh (2003) |
| $\delta^{18}O_{calci}$ | oxygen isotopic composition of unaltered calcite | 1.06 | ‰ PDB | Oehlert and Swart (2014) |
| T | temperature | 15 | °C | |
| $\alpha^{18}O_{calc\text{-}W}$ | Oxygen isotope fractionation factor between calcite and water | 1.031 | | O'Neil et al. (1969) |
| $Ca_{FW}$ | Concentration of Ca in groundwater | 2 | mM | Langmuir (1997); Clark (2015) |
| $Ca_{SW}$ | Concentration of Ca in seawater | 10 | mM | Chester (2012) |
| $^{87}Sr/^{86}Sr_{FW}$ | Sr isotopic compositon of groundwater | 0.7095 | | Clark (2015) |
| $^{87}Sr/^{86}Sr_{SW}$ | Sr isotopic compositon of seawater | 0.708 | | Veizer and others (1999) |
| $^{87}Sr/^{86}Sr_{calci}$ | Sr isotopic compositon of primary calcite | 0.708 | | |
| $K_DSr$ | Partition coefficient of Sr between calcite and fluids | 0.1 | | Zhao and Zheng (2014) |
| $Sr_{FW}$ | Sr concentration of groundwater | $2.5*10^{-3}$ | mM | Langmuir (1997) |
| $Sr_{SW}$ | Sr concentration of seawater | $90*10^{-3}$ | mM | Chester (2012) |
| $Sr_{calci}$ | Sr concentration of primary calcite | 788.58 | ppm | |
| $Mn_{FW}$ | Mn concentration of groundwater | $0.3*10^{-3}$ | mM | Langmuir (1997) |
| $Mn_{SW}$ | Mn concentration of seawater | $0.36*10^{-6}$ | mM | Chester (2012) |
| $K_DMn$ | Partition coefficient of Mn between calcite and fluids | 15 | | Zhao and Zheng (2014) |
| $Mn_{calci}$ | Mn concentration of primary calcite | 0.198 | ppm | |

Note: the $\delta^{13}C_{calci}$ and $\delta^{18}O_{calci}$ values, $Sr_{calci}$, $Mn_{calci}$ and $^{87}Sr/^{86}Sr_{calci}$ ratios of primary calcite were assumed to be equilibrated with seawater.

range of $10^2$ to $10^4$ (Begg and Carter, 1987; Melim and others, 2001; Jones and others, 2004; Caspard and others, 2004), although a much lower value of 2.5 has also been suggested (Kaufman, 1994). The total fluid mass source at the left boundary was set as $2.64 \times 10^{-4}$ kg/($m^2$·s) for the baseline run (table 1), equivalent to a flow rate of ~25 m/yr (Sanford and Konikow, 1989).

The recrystallization rate, endmember compositions of groundwaters and primary carbonates, element partition coefficients, and the isotopic fractionation factor between calcite and fluids used in the baseline runs are shown in table 2. Recrystallization rates during meteoric and mixing zone diagenesis are poorly constrained (Paterson and others, 2008; Avrahamov and others, 2013). However, previous workers have suggested that the transformation from metastable marine carbonate minerals to 100 percent calcite rock during subaerial diagenesis is rapid and could occur over a timescale of 10 to 200 kyr (Matthews, 1968; Steinen and Matthews, 1973; James and Choquette, 1984). This suggests a recrystallization rate on the order of $10^{-6}$ to $10^{-4}$ $yr^{-1}$, which, not surprisingly, is higher than the very low calcite recrystallization rates

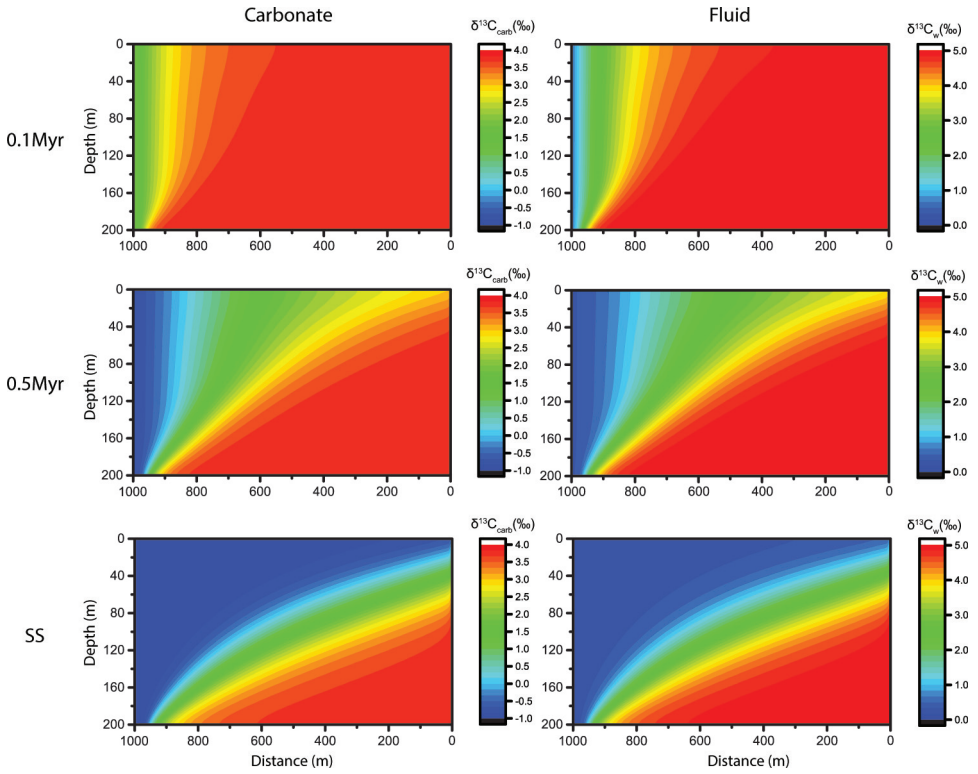


Fig. 2. The time evolution of $\delta^{13}C$ values of calcite and fluid in the whole domain of the baseline run. The left panel represents calcite results, while the right panel represents fluid results. SS represents steady state. See tables 1 and 2 for parameters of this baseline run.

ranging from $2 \times 10^{-8}$ to $4 \times 10^{-7}$ $yr^{-1}$ in deep sea sediments (Fantle and DePaolo, 2007; Fantle, 2015). For the baseline run in this study, the recrystallization rate was set to $10^{-5}$ for the whole model domain. The recrystallization rate decreases with an increase in sedimentary age in deep sea sediments (Fantle and DePaolo, 2006, 2007; Fantle, 2015), which is also likely to occur in the coastal carbonate aquifer.

## Model Results and Discussion

The calculated distribution of salinity values (fig. 1B) and flow directions (fig. 1C) for the baseline run are shown in figure 1. In this run, all the parameters were set within the ranges found in modern carbonate aquifers (tables 1 and 2). Three diagenetic zones, namely the meteoric zone, mixing zone, and marine-burial zone, can be divided according to the distribution of salinities (fig. 1), with the thickness of the mixing zone controlled by dispersion. The calculated flow velocity is faster in the lower-salinity upper portion of the mixing zone, consistent with the findings that the flow velocity and salinity are inversely related (James and Choquette, 1984). We carried out time-dependent runs of carbon isotopes to understand the evolution of the geochemical compositions of both carbonates and fluids in the whole domain (fig. 2). The results show that the composition of fluid and rocks evolve together (fig. 2). The distance to the freshwater source influences the rate of change in carbonate compositions and the steady-state timescale. Carbonate alteration initially begins near the freshwater source (left boundary), and later continues near the seawater boundary

(right boundary) (fig. 2 and fig. A2). This suggests that the magnitude of shifts in carbon and oxygen isotope values may vary within a platform depending on distance from the open ocean if steady state has not been reached, with a larger shift in isotope values expected closer to the freshwater source (fig. 2 and fig. A2). Also, steady state is achieved sooner near the freshwater source than the seawater boundary (fig. 2). Our model simulation indicates that the compositional evolution of the fluid is more rapid than that of the carbonate (fig. 2), and the lag between the two is related to the recrystallization rate, the differences in the concentrations of geochemical components between the fluids and carbonates, distribution coefficients, and flow rates. The lag becomes smaller if the recrystallization rate is high or the flow rate is low.

In the following sections, the model is first applied to simulate alteration of carbon and oxygen isotopic compositions in both modern and ancient carbonate sediments. Then, the model is applied to elemental concentrations of Sr in the carbonate as well as Sr isotope values ($^{87}Sr/^{86}Sr$). We also preformed further sensitivity analyses to understand the controlling factors for rates of change in carbonate elemental and isotopic compositions during alteration. Lastly, one more series of model runs were done to simulate the effects of a downward decrease in recrystallization rate.

### *Application to Carbon and Oxygen Isotopes*

One significant difference between our 2D reactive transport model and previous models (Banner and Hanson, 1990; Jacobsen and Kaufman, 1999; Derry, 2010; Dyer and others, 2017; Ahm and others, 2018) is that this model can simulate the interaction between carbonate sediments and a continuous spectrum of seawater-freshwater mixtures within the mixing zone, while previous models usually simulate water-rock interaction and fluid mixing separately (for example, Banner and Hanson, 1990). We executed time-dependent runs to understand the changes in C and O isotope values in carbonate profiles under different DOAs (fig. 3B) and compared the results with the previously published water-rock interaction and fluid mixing models (Banner and Hanson, 1990). All the parameters used in these 2D runs are within the ranges found in modern carbonate aquifers (fig. 3; tables 1, 2, 3, 4). Consistent with the predictions of Banner and Hanson (1990), the results of the interaction between carbonate and seawater-freshwater mixtures lie between the lines of water-rock interaction and fluid mixing in the cross-plot of $\delta^{18}O_{carb}$ and $\delta^{13}C_{carb}$ values (fig. 3B). As the water-rock ratio of oxygen is much higher than that of carbon, oxygen isotopes achieve steady state more rapidly, after only 0.5 Myr, while $\delta^{13}C_{carb}$ values do not yet reach steady state until 1 Myr (figs. 3C and 3D). In the cross-plot of $\delta^{18}O_{carb}$ and $\delta^{13}C_{carb}$ values, the composition of a selected vertical slice (for example, at 200 m) from the 2D results lies on different curves at different times (figs. 3A and 3B), with DOA increasing with time. At steady state, the result of the interaction between carbonate and seawater-freshwater mixtures exhibits the same trend as the fluid mixing curve (fig. 3B), with the curvature related to the DIC concentration ratio between freshwater and seawater. The steady-state mixing curve would be a straight line if the DIC concentration of freshwater and seawater were equal (figs. 4, 5, and 6).

Water-rock interaction models produce an L-shape or inverted J curve for the relationship between $\delta^{13}C_{carb}$ and $\delta^{18}O_{carb}$ values during alteration by a single fluid (Lohmann, 1987; Banner and Hanson, 1990; Banner and Kaufman, 1994; Banner, 1995; Jacobsen and Kaufman, 1999), which has been mistakenly used to suggest that a positive correlation between $\delta^{13}C_{carb}$ and $\delta^{18}O_{carb}$ values is not significant evidence for diagenetic overprint of the $\delta^{13}C_{carb}$ (see Derry, 2010 for the discussion of this phenomenon). For the interaction between carbonate sediments and seawater-freshwater mixtures, Banner and Hanson (1990) have suggested that the resulting carbonate would lie between the water-rock interaction and seawater-freshwater mix-

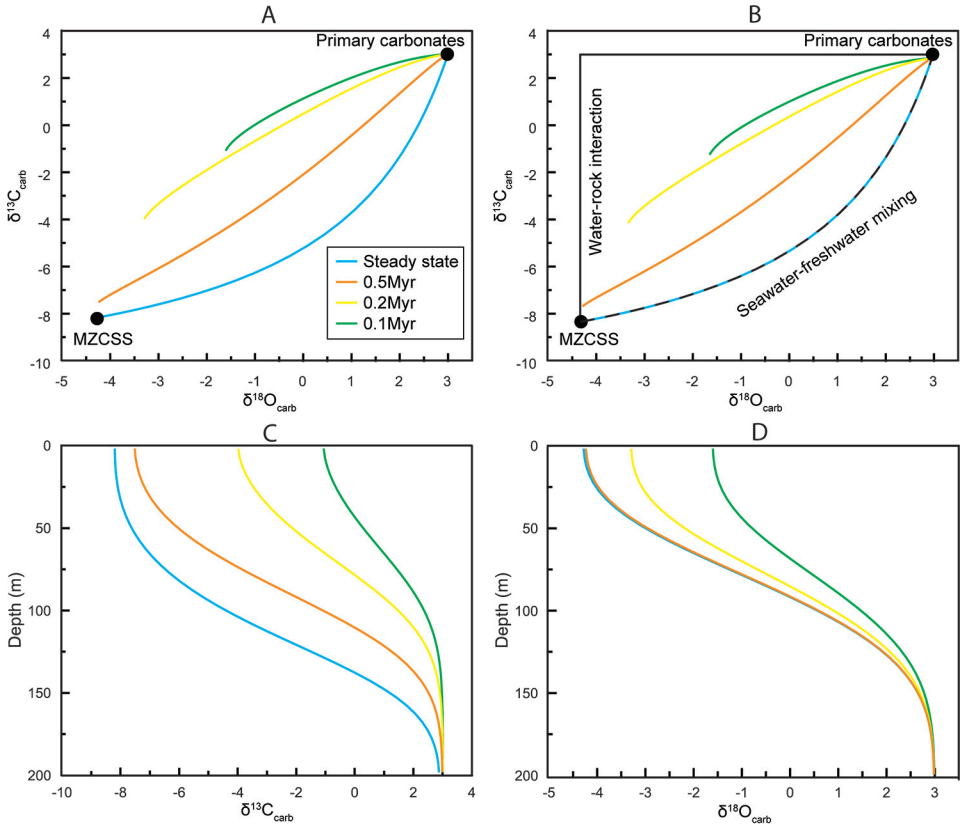


Fig. 3. A comparison between the water-rock interaction model and the 2D reactive transport model. (A) Time evolution of the relationships between carbon and oxygen isotopes from 2D reactive transport model. (B) A comparison between the results of the 2D reactive transport model and those of the water-rock interaction model (Banner and Hanson, 1990) and the fluid endmember mixing. (C) Time evolution of carbonate carbon isotopic profiles. (D) Time evolution of carbonate oxygen isotopic profiles. The result for the 2D reactive transport model is the vertical slice at 200 m. See table 3 for the parameters. MZCSS represent meteoric zone carbonates at steady state.

ing curves (fig. 3). Results from Derry's (2010) water-rock interaction model suggest that burial diagenetic fluids with high $pCO_2$ were required to generate the positive correlations between carbonate carbon and oxygen isotope values that characterize the Shuram-Wonoka anomaly. However, by directly simulating the interaction between carbonate and a continuous spectrum of a seawater-freshwater mixture in the mixing zone, we find that a linear relationship between carbon and oxygen isotopes can be generated during these simulations without high $pCO_2$ (figs. 3, 4 and 6). This observation can explain the positive correlation between carbon and oxygen isotope values observed in the rock record, such as those in modern Great Bahama Bank and the Neoproterozoic Shuram-Wonoka anomaly (figs. 4 and 5, and fig. A3). The different slopes of the correlation between $\delta^{13}C_{carb}$ and $\delta^{18}O_{carb}$ values in the Shuram-Wonoka anomaly can be reproduced by different endmember compositions of groundwater and marine pore waters (fig. 4). In the runs simulating these shifts in C and O isotope values (figs. 4 and 5), the $\delta^{13}C_{carb}$ and $\delta^{18}O_{carb}$ of groundwater and seawater were assumed to be in equilibrium with those of altered and primary carbonates,

TABLE 3

*Values of parameters used in each figure*

| parameters | units | Fig. 2, Fig. 4a-c | Fig.3 | Fig.4d-f (Shuram) | Fig.4d-f (Wonoka) | Fig. 5 | Fig. 6a | Fig. 6b |
|---|---|---|---|---|---|---|---|---|
| $\rho$ | $g/cm^3$ | 2.6 | 2.6 | 2.6 | 2.6 | 2.6 | 2.6 | 2.6 |
| R | $yr^{-1}$ | $1*10^{-5}$ | $1*10^{-5}$ | $1*10^{-5}$ | $1*10^{-5}$ | $1*10^{-5}$ | $1*10^{-5}$ | $1*10^{-5}$ |
| $\delta^{13}C_{FW}$ | ‰ | 0.3 | -7 | -9 | -8.5 | -7 | -12 | -12 or 11.2 |
| $DIC_{FW}$ | mM | 1.2 | 9.2 | 2.3 | 2.3 | 1.2 | 1 | 1 |
| $DIC_{SW}$ | mM | 2.3 | 2.3 | 2.3 | 2.3 | 2.3 | 1 | 1 |
| $\delta^{13}C_{calci}$ | ‰ | 3.8 | 3.0 | 3.5 | -0.8 | 5 | 10 | 10 |
| $\alpha^{13}C_{calc\text{-}W}$ | | 0.9988 | 0.9988 | 0.9988 | 0.9988 | 0.9988 | 0.9988 | 0.9988 |
| $\delta^{18}O_{FW}$ | ‰ SMOW | -2.5 | -4 | -8 | -14 | -7 | -12 | -12 |
| $\delta^{18}O_{calci}$ | ‰ PDB | 1.06 | 3 | -2 | -5.5 | -1.3 | 5 | 5 |
| T | °C | 15 | 15 | 15 | 15 | 15 | 15 | 15 |
| $\alpha^{18}O_{calc\text{-}W}$ | | 1.031064 | 1.031064 | 1.031064 | 1.031064 | 1.031064 | 1.031064 | 1.031064 |
| $Ca_{FW}$ | mM | - | - | - | - | 2 | - | - |
| $Ca_{SW}$ | mM | - | - | - | - | 10 | - | - |
| $^{87}Sr/^{86}Sr_{FW}$ | | - | - | - | - | 0.70895 | - | - |
| $^{87}Sr/^{86}Sr_{SW}$ | | - | - | - | - | 0.70865 | - | - |
| $^{87}Sr/^{86}Sr_{calci}$ | | - | - | - | - | 0.708 | - | - |
| $K_DSr$ | | - | - | - | - | 0.0065 | - | - |
| $Sr_{FW}$ | mM | - | - | - | - | $3.5*10^{-3}$ | - | - |
| $Sr_{SW}$ | mM | - | - | - | - | $90*10^{-3}$ | - | - |
| $Sr_{calci}$ | ppm | - | - | - | - | 788.58 | - | - |
| $Mn_{FW}$ | mM | - | - | - | - | - | - | - |
| $Mn_{SW}$ | mM | - | - | - | - | - | - | - |
| $K_DMn$ | | - | - | - | - | - | - | - |
| $Mn_{calci}$ | ppm | - | - | - | - | - | - | - |
| parameters | units | Figs.7-8 | Fig.9a,b | Fig.9c,d | Fig.9e,f | Fig.9g,h | Fig.10 | Fig.11 |
| $\rho$ | $g/cm^3$ | 2.6 | 2.6 | 2.6 | 2.6 | 2.6 | 2.6 | 2.6 |
| R | $yr^{-1}$ | $1*10^{-5}$ | $1*10^{-5}$ | $1*10^{-5}$ | $1*10^{-5}$ | $1*10^{-5}$ or $1*10^{-6}$ | $1*10^{-5}$ | Decrease with depth |
| $\delta^{13}C_{FW}$ | ‰ | 0.3 | - | - | - | - | - | -0.2 |
| $DIC_{FW}$ | mM | 1.2 | - | - | - | - | - | 1.2 |
| $DIC_{SW}$ | mM | 2.3 | - | - | - | - | - | 2.3 |
| $\delta^{13}C_{calci}$ | ‰ | 3.8 | - | - | - | - | - | 3.8 |
| $\alpha^{13}C_{calc\text{-}W}$ | | 0.9988 | - | - | - | - | - | 0.9988 |
| $\delta^{18}O_{FW}$ | ‰ SMOW | -4 | - | - | - | - | - | -2.5 |
| $\delta^{18}O_{calci}$ | ‰ PDB | 3 | - | - | - | - | - | 1.06 |
| T | °C | 15 | - | - | - | - | - | 15 |
| $\alpha^{18}O_{calc\text{-}W}$ | | 1.031064 | - | - | - | - | - | 1.031064 |
| $Ca_{FW}$ | mM | 2 | 2 | 2 or 6 | 2 | 2 | 2 | - |
| $Ca_{SW}$ | mM | 10 | 10 | 10 | 10 | 10 | 10 | - |
| $^{87}Sr/^{86}Sr_{FW}$ | | 0.7095 | 0.7095 | 0.7095 | 0.7095 | 0.7095 | 0.7095 | - |
| $^{87}Sr/^{86}Sr_{SW}$ | | 0.708 | 0.708 | 0.708 | 0.708 | 0.708 | 0.708 | - |
| $^{87}Sr/^{86}Sr_{calci}$ | | 0.708 | 0.708 | 0.708 | 0.708 | 0.708 | 0.708 | - |
| $K_DSr$ | | 0.1 | 0.1 | 0.1 | 0.1 or 0.02 | 0.1 | 0.1 | - |
| $Sr_{FW}$ | mM | $2.5*10^{-3}$ | $2.5*10^{-3}$ or $2.5*10^{-2}$ | $2.5*10^{-3}$ | $2.5*10^{-3}$ | $2.5*10^{-3}$ | $2.5*10^{-3}$ | - |
| $Sr_{SW}$ | mM | $90*10^{-3}$ | $90*10^{-3}$ | $90*10^{-3}$ | $90*10^{-3}$ | $90*10^{-3}$ | $90*10^{-3}$ | - |
| $Sr_{calci}$ | ppm | 788.58 | 788.58 | 788.58 | 788.58 | 788.58 | 788.58 | - |
| $Mn_{FW}$ | mM | $0.3*10^{-3}$ | - | - | - | - | - | - |
| $Mn_{SW}$ | mM | $0.36*10^{-6}$ | - | - | - | - | - | - |
| $K_DMn$ | | 15 | - | - | - | - | - | - |
| $Mn_{calci}$ | ppm | 0.198 | - | - | - | - | - | - |

Note: 1. Other than fig. 5 and fig. 10, the hydrology parameters for all these figures are the same with the baseline run shown in table 1.

2. For fig. 5 and fig. 10, the hydrology parameters that are different from the baseline run are listed in the figure or figure captions.

respectively. Note that the calculated C and O isotopic values of groundwater during the Neoproterozoic Shuram-Wonoka anomaly are within the ranges of modern groundwater compositions (table 4).

TABLE 4

*Ranges of selected parameters in modern natural condition*

| parameter | description | values | units | references |
|---|---|---|---|---|
| $DIC_{FW}$ | DIC concentration of groundwater | 0.1 to 20 | mM | Langmuir (1997) |
| $\delta^{13}C_{FW}$ | carbon isotope composition of groundwater | -14 to -1 | ‰ PDB | Appelo and others (2004); Clark (2015) |
| $\delta^{18}O_{FW}$ | oxygen isotopic composition of groundwater | -25 to 0 | ‰ SMOW | Appelo and others (2004); Clark (2015) |
| $Ca_{FW}$ | Concentration of Ca in groundwater | 0.02 to 10 | mM | Langmuir (1997); Clark (2015) |
| $^{87}Sr/^{86}Sr_{FW}$ | Sr isotopic compositon of groundwater | 0.707 to >0.71 | | Clark (2015) |
| $K_DSr$ | Partition coefficient of Sr between carbonates and fluids | 0.005 to 0.2 | | Vahrenkamp and Swart (1990); Zhao and Zheng (2014) |
| $Sr_{FW}$ | Sr concentration of groundwater | $3*10^{-4}$ to 0.3 | mM | Langmuir (1997) |
| $v_{FW}$ | Groundwater discharge rate | <2 to >250 | m/yr | Sanford and Konikow (1989); Caspard and others (2004); Rezaei and others (2005) |

The 2D model can also be applied to stratigraphic trends of $\delta^{13}C_{carb}$ and $\delta^{18}O_{carb}$ values. Thus, vertical slices were picked from the 2D results to compare with natural stratigraphic variations in modern and ancient deposits (figs. 4 and 5, and fig. A3), which show gradual shifts of $\delta^{13}C_{carb}$and $\delta^{18}O_{carb}$ values across the mixing zone. The thicknesses of the intervals characterized by shifts in $\delta^{13}C_{carb}$ and $\delta^{18}O_{carb}$values in the Shuram-Wonoka anomaly (~15–100 m, figs. 4 and 5) also fall within the range of thicknesses found in the mixing zones of the modern Great Bahama Bank and in Triassic strata (<10 m to ~100 m, Melim and others, 2002, 2004; Zhao and Zheng, 2017; Swart and Oehlert, 2018). Positive correlations between $\delta^{13}C_{carb}$ and $\delta^{18}O_{carb}$ values can also be generated by mixing varying proportions of minerals, such as aragonite and calcite, or calcite and dolomite (Zhao and Zheng, 2017; Swart and Oehlert, 2018). However, in the case of mineral mixing, point-to-point differences in $\delta^{13}C_{carb}$ and $\delta^{18}O_{carb}$ values between successive stratigraphic samples are often pronounced (Zhao and Zheng, 2017), as opposed to the smooth stratigraphic expression resulting from correlations driven by freshwater and seawater mixing.

It has been commonly suggested that a lack of linear positive correlation between $\delta^{13}C_{carb}$ and $\delta^{18}O_{carb}$ values is sufficient to rule out meteoric diagenesis (for example, Swanson-Hysell and others, 2010; Metzger and Fike, 2013). Our approach demonstrates that non-linear relationships between $\delta^{13}C_{carb}$ and $\delta^{18}O_{carb}$ may be generated through the interaction between carbonate sediments and a continuous spectrum of seawater-freshwater mixtures, which lie between lines of water-rock interaction and fluid mixing (figs. 3, 4 and 6). The curvature of the steady-state mixing curves is controlled by the ratio between freshwater DIC concentration and seawater DIC concentration (figs. 3, 4 and 6). This observation supports the interpretation by previous workers who also found that water-rock interaction and fluid mixing may result in nonlinear relationships (Banner and Hanson, 1990; Marshall, 1992).

More importantly, the lack of a linear positive correlation between $\delta^{13}C_{carb}$ and $\delta^{18}O_{carb}$ values can actually reflect a complex diagenetic history. For example, it may indicate meteoric and mixing-zone diagenesis during several deposition and exposure cycles (that is, Swart and Oehlert, 2018). Each of these cycles may have had a different

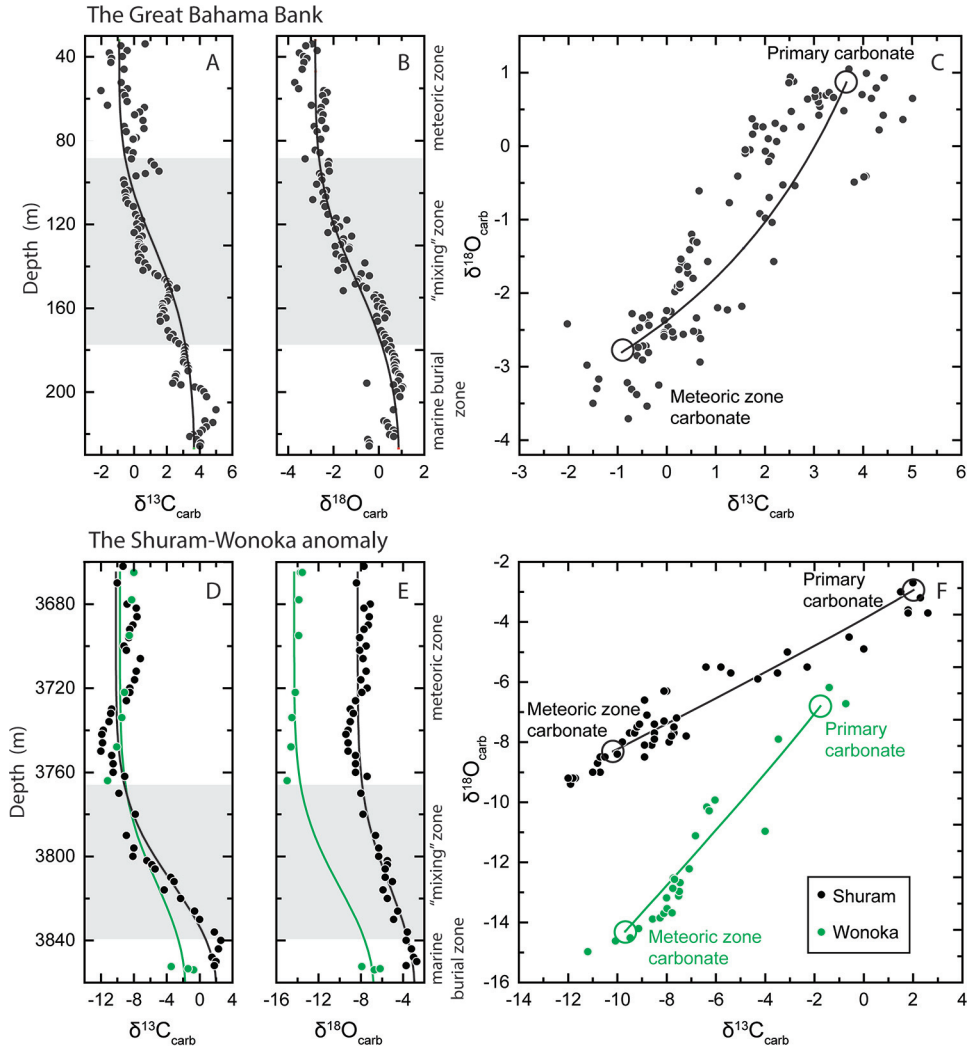


Fig. 4. Model results for shifts in $\delta^{13}C_{carb}$ and $\delta^{18}O_{carb}$ values from the Clino core of the Great Bahama Bank (A-C) and the Shuram-Wonoka anomaly (D-F). The profile is divided into three diagenetic zones: the marine burial zone, the mixing zone, and the meteoric zone. The model results for the Great Bahama Bank is the vertical slice at 500 m from the baseline run with steady-state $\delta^{13}C_{carb}$ and $\delta^{18}O_{carb}$ values. See table 1 and 2 for parameters. The model results of the Shuram-Wonoka anomaly is the vertical slice at 700 m. See table 3 for the parameters. The $\delta^{13}C_{carb}$and $\delta^{18}O_{carb}$ values for the Great Bahama Bank, the Shuram anomaly, and the Wonoka anomaly came from Oehlert and Swart (2014), Fike and others (2006) and Calver (2000), respectively.

DOA or different $\delta^{13}C$ value for groundwater. This interpretation may be applicable to the C and O isotopic data of the Neoproterozic Trezona anomaly (fig. 6) in the Australia (Swanson-Hysell and others, 2010). We further support this possibility through time-dependent runs similar to those of figure 3, with the C and O isotopic compositions of groundwater and seawater assumed to be in equilibrium with those of altered and primary carbonate endmembers suggested by the data (fig. 6). The data of the Neoproterozic Trezona anomaly lies in a region between lines of water-rock interaction and fluid mixing, which can be explained by the interaction between

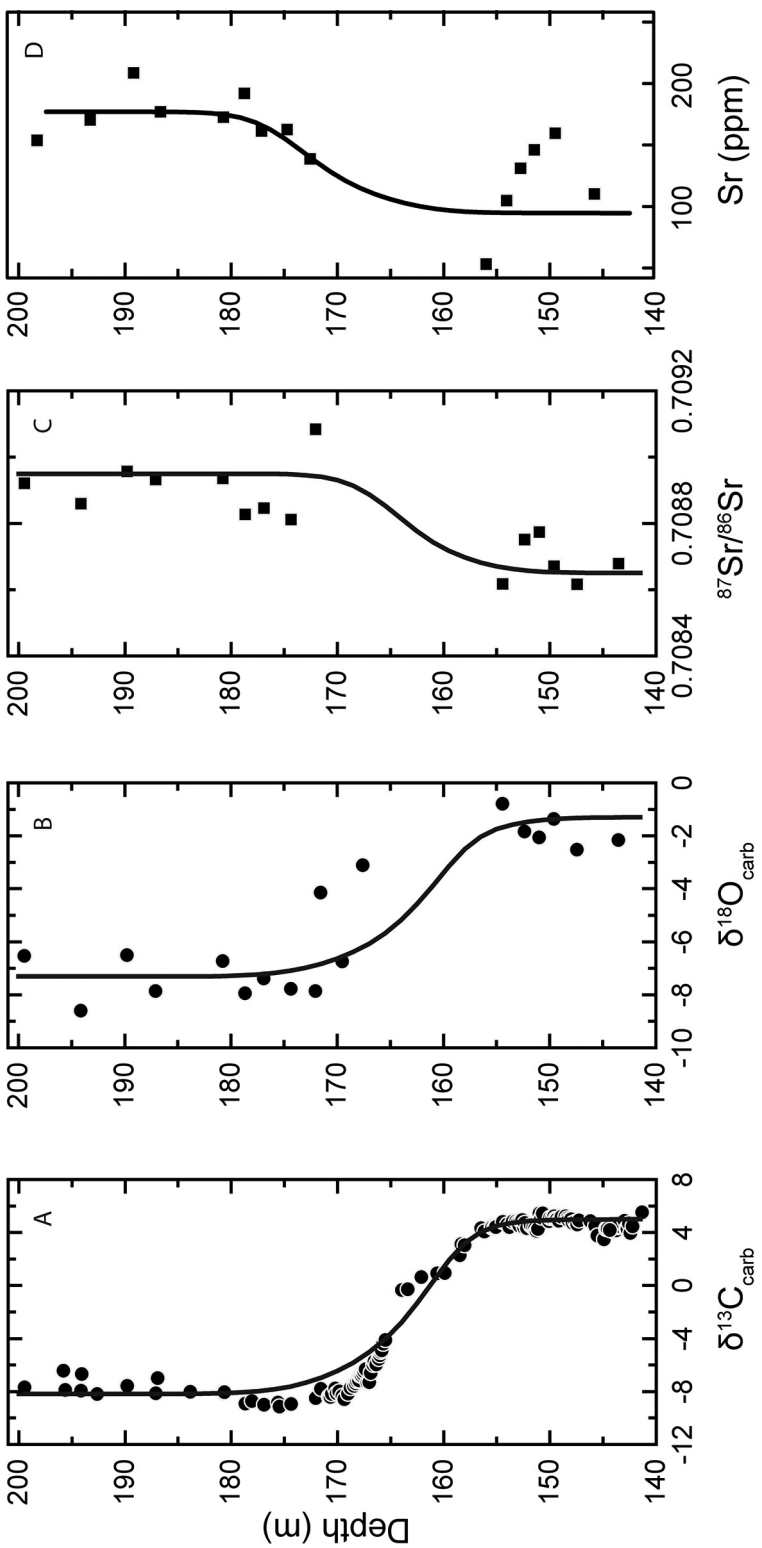


Fig. 5. Model results for the shifts in $\delta^{13}C$, $\delta^{18}O$, $[Sr]_{carb}$ and $^{87}Sr/^{86}Sr$ of the Shuram anomaly, recorded in carbonates from the Doushantuo Formation in South China. The domain of this run is 60m high with 40 layers and 1000 m long with 100 layers. The used model domain is thinner than the other runs, as the mixing zone is thin (~15 m) in the Doushantuo Formation, with $D_m = 1*10^{-8}$ $m^2/s$ and $Q_N = 2.667*10^{-4}$ $kg/(m^2s)$. The other parameters can be found in tables 1 and 3. The model is run to steady state for carbonate $\delta^{13}C$, $\delta^{18}O$, and $^{87}Sr/^{86}Sr$ values. The plotted model results came from the vertical slice at 300 m. The data came from Sawaki and others (2010).

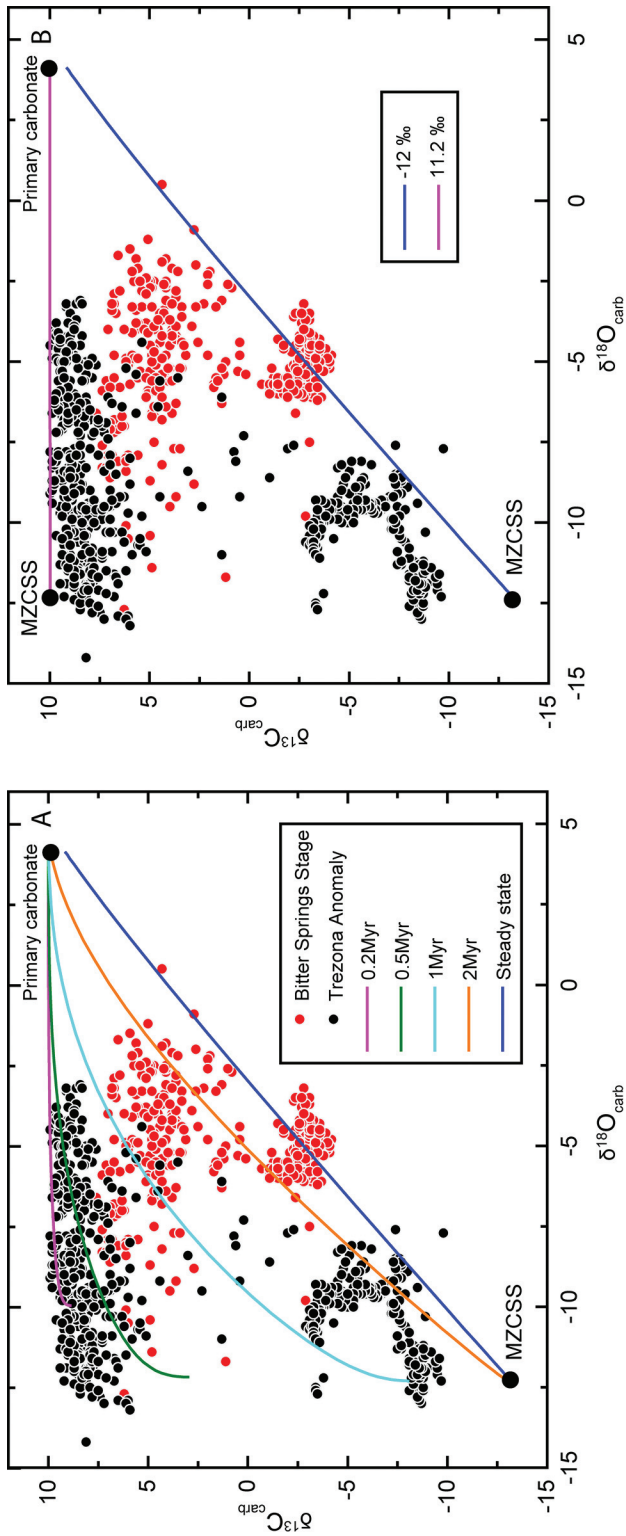


Fig. 6. Model results for the Neoproterozoic Trezona Anomaly. (A) Model results with different degrees of alteration (that is, results of the same run at different times) for the Trezona Anomaly. (B) Model results with different $\delta^{13}C$ values for groundwater for the Trezona Anomaly, with all the other parameters the same with A. The plotted model results came from the vertical slice at 500 m. See table 3 for the parameters. The data for the Trezona anomaly came from Swanson-Hysell and others (2010). MZCSS represent meteoric zone carbonates at steady state.

carbonate sediments and a continuous spectrum of seawater-freshwater mixtures with various DOAs (fig. 6A). The data can also be explained by variations in $\delta^{13}C$ values of groundwaters during each exposure cycle (fig. 6B). Again, in these simulations, the inferred endmember C and O isotopic values of groundwater are within the ranges of modern groundwater compositions (table 4).

*Model Application to [Sr], [Mn] and Sr Isotopes*

This model may also be applied to evaluate the behavior of the other elements and isotopes during diagenesis. To demonstrate the utility of the model beyond C-O isotope values, we conducted model runs to explore what conditions could drive observed variations in carbonate Sr concentration and isotopic composition in the Shuram anomaly interval in the Doushantuo Formation (fig. 5 and table 3). Assuming that the Sr and Ca concentrations of the Ediacaran seawater are the same with those of modern seawater, a Sr distribution coefficient ($K_D$Sr) of 0.0065 was then applied to match the Sr concentration (~100 ppm) of carbonate below the Shuram anomaly interval (fig. 5). Assuming that Sr exchange equilibrium has been reached between altered carbonate and groundwater, the Sr/Ca of the groundwater was then calculated using the $K_D$Sr (0.0065) and the Sr concentration (~170 ppm) of altered carbonate in the Shuram anomaly interval (fig. 5). The increase in the $^{87}Sr/^{86}Sr$ ratio is interpreted here to reflect the influence of meteoric water, which has a higher $^{87}Sr/^{86}Sr$ ratio than (0.70895) that of seawater (0.70865). With the application of these constraints (fig. 5 and table 3), the variations in Sr concentration and Sr isotopic compositions across the sedimentary profile can be reproduced by running the model to steady state (fig. 5). Depending on the rock type through which the groundwater has recharged, the $^{87}Sr/^{86}Sr$ ratio of groundwater may have a large range (0.707 to >0.71, Clark, 2015). This may leave a strong regional signal in the $^{87}Sr/^{86}Sr$ ratio of carbonates after meteoric diagenesis. Variations in the Sr concentration of carbonates after meteoric diagenesis could be more complex, as there are changes in distribution coefficients during aragonite to calcite transformation or dolomitization (for example, Melim and others, 2002). Thus, the increase in Sr concentration in the interval with a negative carbon isotopic shift (fig. 5) could be due to dolomite to calcite transformations (Sawaki and others, 2010) and/or a higher Sr/Ca of groundwater relative to that of seawater (for example, Clark, 2015).

Another series of model runs were conducted to understand 1) the difference in rates of change of different geochemical components in altered carbonates; and 2) the relationships between these elemental and isotopic systems and carbonate oxygen isotopes. The evolution of the concentration of trace elements (such as Sr and Mn) and isotopes (such as Sr isotopes) in sedimentary profiles were calculated (fig. 7) using values of parameters within the ranges of those of modern carbonate aquifers (tables 3 and 4). The results of the model suggest that at any given time, there are likely to be varying DOAs between different geochemical components of carbonates. Oxygen isotopes are among the first to achieve steady state (figs. 7 and 8), while Mn requires the longest time to reach steady state (fig. 7 and A4). For instance, with the baseline recrystallization rate, the Mn concentration of calcite at the 500m slice does not change before 2Myr (fig. 7). This is because the fluid Mn concentration is strongly buffered by the carbonate near the freshwater source (fig. A4). The DOA can also vary at different depths of the same profile for each time slice (fig. A5). The cross-plots between different components and $\delta^{18}O_{carb}$ values show curves with different DOAs rather than straight lines (fig. 8). Note that the stratigraphic position of shifts could vary among different components due to fluid mixing (fig. 7).

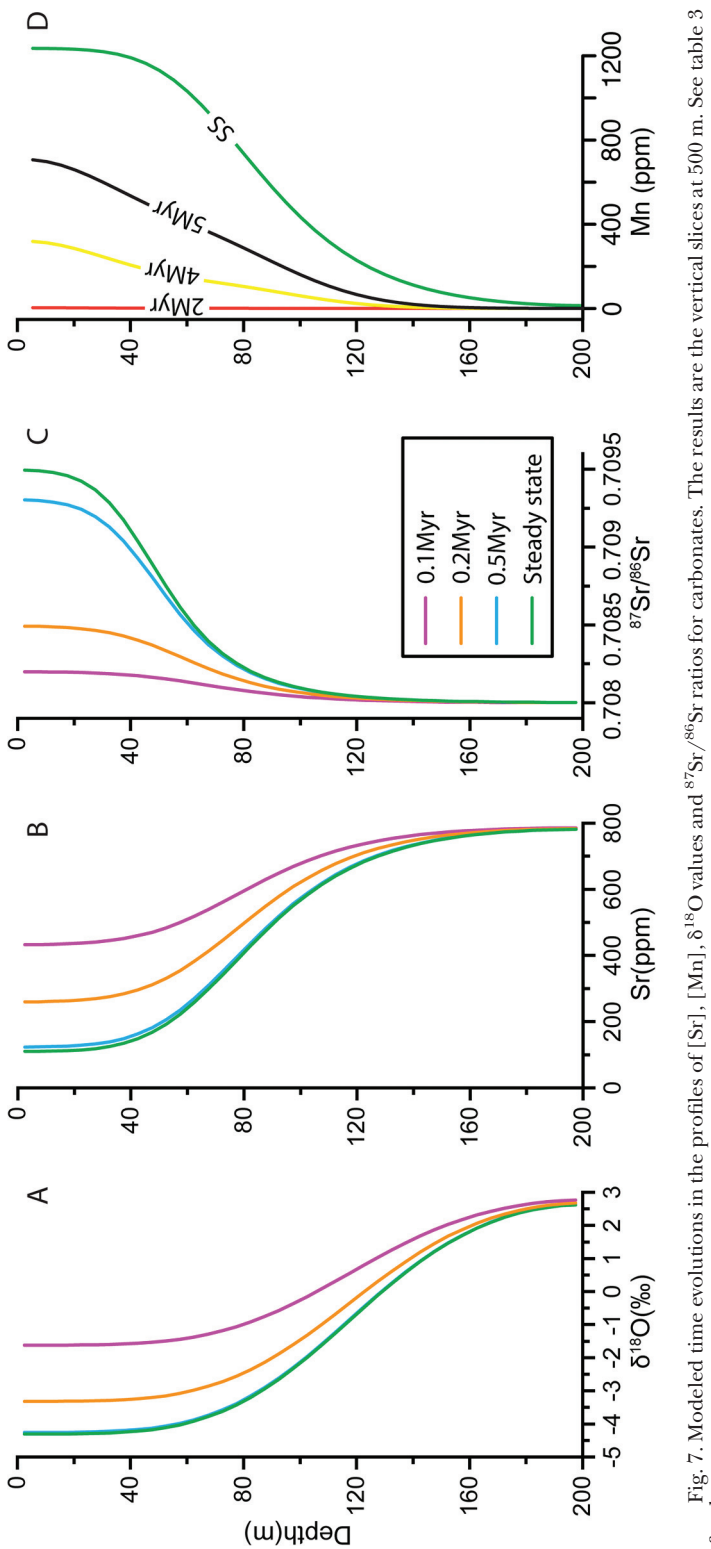


Fig. 7. Modeled time evolutions in the profiles of [Sr], [Mn], $\delta^{18}O$ values and $^{87}Sr/^{86}Sr$ ratios for carbonates. The results are the vertical slices at 500 m. See table 3 for the parameters.

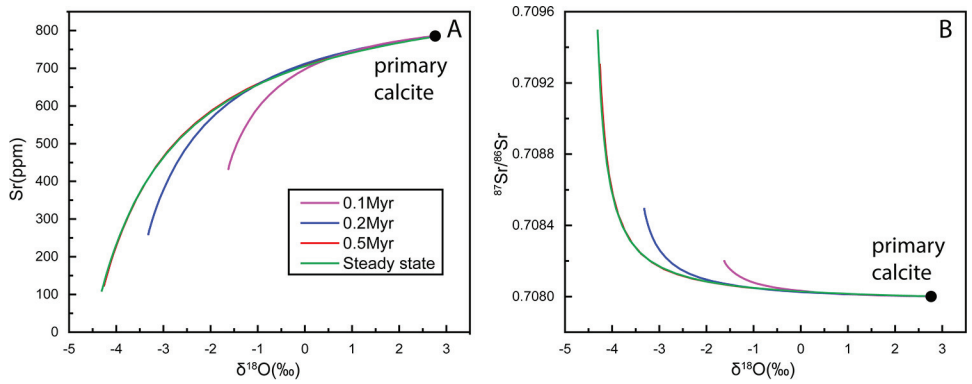


Fig. 8. Modeled relationships between $^{87}Sr/^{86}Sr$ ratios, [Sr] and $\delta^{18}O$ values of a selected vertical slice at different times, for the same model runs presented in fig. 7. The results are the vertical slices at 500 m. Note that the 0.5 Myr curve is very similar to the steady-state curve.

*Controlling Factors for the Rate of Change in Carbonate Compositions During Alteration*

We use Sr concentrations and $^{87}Sr/^{86}Sr$ ratios to explore factors influencing the rate of change in carbonate compositions during alteration (figs. 9 and 10). In this exercise, we have varied the geochemical compositions of groundwater, the distribution coefficient, the recrystallization rate, and the hydrology parameters (tables 3 and 4). The rate of change in carbonate compositions and the steady-state timescale are negatively correlated, with higher rate of change corresponding to shorter steady-state timescales. The model results show that the rate of change of both the concentration of Sr and the $^{87}Sr/^{86}Sr$ ratios during alteration is controlled by compositional differences between fluid endmembers (figs. 9B, 9C, and 9D), the calcite-water element distribution coefficient (figs. 9E and 9F), recrystallization rate (figs. 9G and 9H), groundwater discharge rate (figs. 10A and 10B) and porosity. For example, the rate of change of Sr concentration in altered calcite is controlled by the Ca concentration ratio between the fluid endmembers, and this rate of change increases following an increase in Ca concentration in groundwater relative to that of marine pore water (fig. 9C). This is similar to results from the Banner and Hanson (1990) water-rock interaction model, which suggest that the fluid/rock ratio for a given DOA is inversely correlated with the Ca concentration of the fluid. The rate of change of Sr isotopic composition in altered carbonates is positively correlated with the Sr concentration ratio between groundwater and marine pore water (fig. 9B), and it is negatively correlated with the Ca concentration ratio between groundwater and marine pore water (fig. 9D). This indicates that the rate of change of Sr isotopic composition in altered carbonates will increase at higher Sr/Ca ratios of groundwater. Consistent with conclusions based on the water-rock interaction model (Banner and Hanson, 1990), the rate of change of both the Sr concentration and isotopic composition of altered calcite decreases as the calcite-water element distribution coefficient increases (figs. 9E and 9F). Thus, elements with a high calcite-water element distribution coefficient ($>10$), such as Mn and rare earth elements (REEs) (for example, Zhao and Zheng, 2014), are well buffered and so take much longer to be altered (fig. 7 and fig. A4). Intuitively, the rate of change of both the Sr concentration and isotopic composition of altered calcite increases following an increase in recrystallization rates and/or groundwater discharge rate (figs. 9G, 9H, 10A and 10B). The steady-state timescale increases with a decrease in recrystallization rate (figs. 9G and 9H), and vice versa.

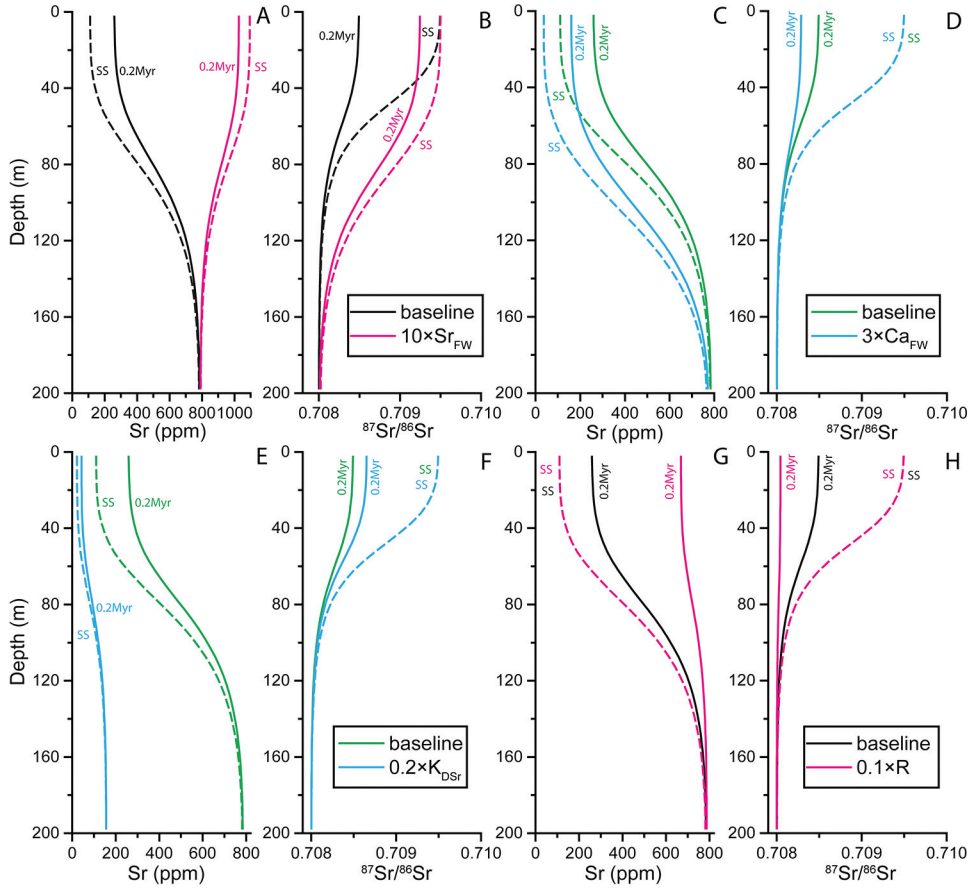


Fig. 9. The influence of non-hydrological factors on the rates of change of Sr and Sr isotopes in limestone profiles during alteration. (A, B) The influence of Sr concentration, with a 10x increase in the Sr concentration of freshwater ($Sr_{FW}$) when compared to the baseline run. (C, D) The influence of Ca concentration, with a 3x increase in the Ca concentration of freshwater ($Ca_{FW}$). (E, F) The influence of the distribution coefficient ($K_{DSr}$) between calcite and water. (G, H) The influence of recrystallization rates. The results are the vertical slices at 500 m. The solid lines represent results at 0.2 Myr, while the dotted lines represent steady-state results. See table 3 for the parameters.

Previous modeling studies of water-rock interaction reveal that the rate of change in carbonate compositions during alteration are functions of the elemental concentration ratio between carbonate and fluid, open vs. closed system behavior, porosity, and the distribution coefficients (Land, 1980; Banner and others, 1988; Banner and Hanson, 1990; Wang and Cerling, 1994; Maliva, 1998). In our reactive transport model, the recrystallization rate and the groundwater discharge rate are parameterized and are also found to be important for the rate of change in carbonate compositions during alteration. From a practical point of view, the groundwater discharge rate in the reactive transport model is linked to the concept of open vs. closed system behavior in the water-rock interaction model, with high groundwater discharge rate corresponding with 'open systems' and vice versa.

### *Decrease in Recrystallization Rate with Depth in Phreatic Zone*

Based on an evaluation of the depth of the ancient phreatic zone in the Great Bahama Bank, Swart and Oehlert (2018) suggested that the co-variation of carbonate

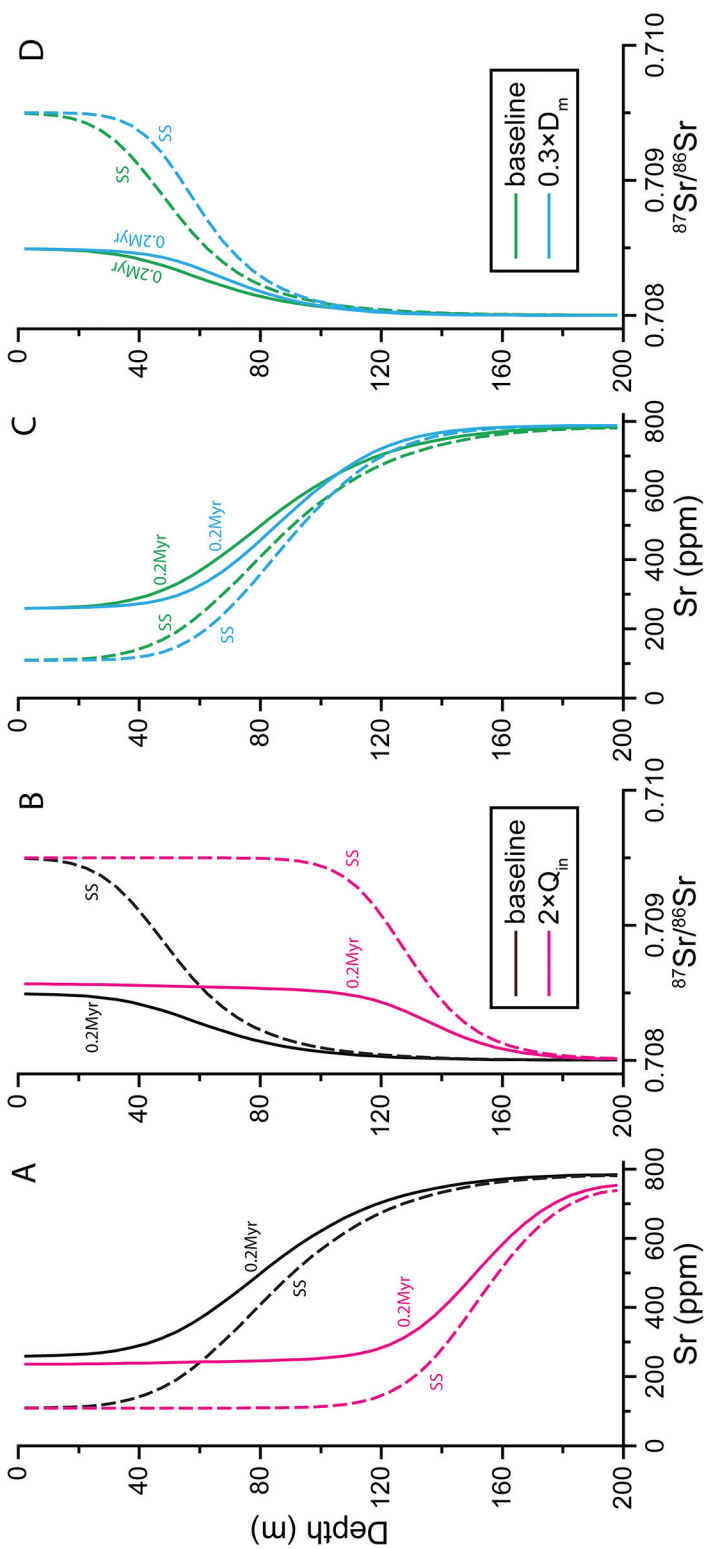


Fig. 10. The influence of hydrology parameters on the rates of change of Sr and Sr isotopes in limestone profiles during alteration. (A, B) The influence of freshwater discharge rates. (C, D) The influence of dispersion. The results are the vertical slices at 500 m. The other parameters can be found in table 3.

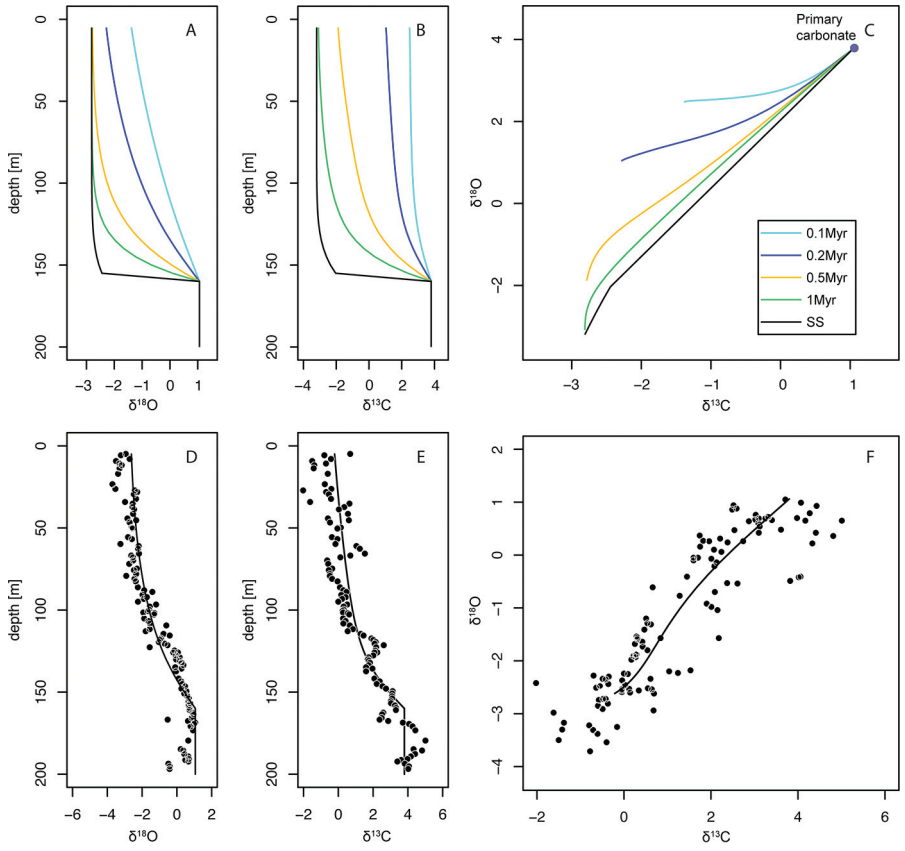


Fig. 11. Time evolution of carbon and oxygen isotopic profiles with a downward decrease in recrystallization rate in the phreatic zone. (A) Time evolution of carbonate carbon isotopic profiles. (B) Time evolution of carbonate oxygen isotopic profiles. (C) Time evolution of the relationships between carbon and oxygen isotopes. (D–F) An application to the Clino core of the Great Bahama Bank. The recrystallization rate was set to the baseline value at the top of the model domain and to zero at the bottom of the phreatic zone, with a linear decrease with depth between them (fig. A8). The recrystallization rate was set as zero in the mixing zone and marine burial zone (fig. A8). The other parameters are shown in table 3. The results shown are from the vertical slice at 850 m. Model results in (D–F) are at 0.3 Myr.

carbon and oxygen isotopes in the Clino core could be generated in the freshwater phreatic zone as a result of a decrease in the DOA from the top of phreatic zone downward. To explore this hypothesis, we did a series of runs with a linear decrease of recrystallization rate from the top to the bottom of the phreatic zone (the meteoric zone in fig. 1D). The recrystallization rate was set to a fixed value at the top, and to zero at the bottom of the phreatic zone (fig. A8). In the mixing zone and the marine burial zone, the recrystallization rate was set to zero. The results are shown in figure 11 and figures A8-A12. Consistent with Swart and Oehlert (2018), our model simulation with a downward decreasing trend in the recrystallization rate of the phreatic zone can also generate the pattern of carbonate carbon and oxygen isotopic variations seen in the Clino core (fig. 11). An additional simulation suggests that dissolution in the mixing zone (Swart and Oehlert, 2018) won't have much influence on the isotopic composition of carbonate in the phreatic zone (fig. A10). Therefore, our model results support the idea that, in addition to fluid mixing, changes in the recrystallization rate may also

be able to produce the positive correlations between carbonate carbon and oxygen isotopic compositions.

The factors controlling the rates of change in carbonate compositions during alteration are the same in both the recrystallization and mixing scenarios (figs, 9, A13 and A14). The scenario with varied recrystallization rates in the phreatic zone requires a very long time (usually >10 Myr) to reach steady state for the applied recrystallization rates. The rates of change in carbonate compositions during alteration also vary among different elements and isotopes (fig. A11). Shifts in elemental and isotopic compositions always start from the bottom of the phreatic zone (fig. A11), as no recrystallization was set below. The relationships between carbonate components and oxygen isotopes are also curves, but are nearly straight lines for some components, such as carbonate Sr concentrations (fig. A12).

## CONCLUSIONS

In contrast to previous studies, we have produced a 2D reactive transport model which simulates the interaction between carbonates and a continuous spectrum of seawater-freshwater mixtures. The model can also be used to calculate the spatiotemporal variations of carbonate compositions during meteoric and mixing-zone diagenesis. The simulated results of the interaction between carbonate and seawater-freshwater mixtures lie between the lines of water-rock interaction and fluid mixing in the cross-plot of $\delta^{18}O_{carb}$ and $\delta^{13}C_{carb}$values. Our model suggests that linear co-variations between $\delta^{13}C_{carb}$ and $\delta^{18}O_{carb}$ values observed in recently meteorically altered shallow-water carbonate successions can be generated in the mixing zone of freshwater and marine pore water or in the freshwater phreatic zone due to a downward decrease in recrystallization rate. Sensitivity analyses indicate that the final composition of carbonates after meteoric and/or mixing-zone diagenesis depends on hydrology, recrystallization rates, the compositions of the groundwater and marine pore water, element partition coefficients and isotopic fractionation factors between carbonate and fluids, the degree of alteration, and the distance from freshwater sources. Further, numerous processes, including fluid mixing and complex diagenetic histories, may decouple $\delta^{18}O_{carb}$ values from other isotopic and elemental signatures during carbonate diagenesis, indicating that a lack of linear correlation with $\delta^{18}O_{carb}$ values does not necessarily suggest limited meteoric alteration. Additionally, our diagenetic model can reproduce 'enigmatic features' of Neoproterozoic negative carbon isotope excursions that have been previously linked to either major global biogeochemical perturbations or diagenetic alteration (for example, the Shuram-Wonoka anomaly; Bristow and Kennedy, 2008). Finally, we suggest that application of the presented reactive transport model to multiple geochemical systems can help evaluate depositional and diagenetic interpretations of carbonate geochemical anomalies.

## ACKNOWLEDGMENTS

We are extremely grateful to Cerys Holstege, Fiona Whitaker, Peter Swart, Brennan O'Connell, Catherine Wise and Shuang Zhang for their useful suggestions. We acknowledge the constructive reviews of the reviewers.

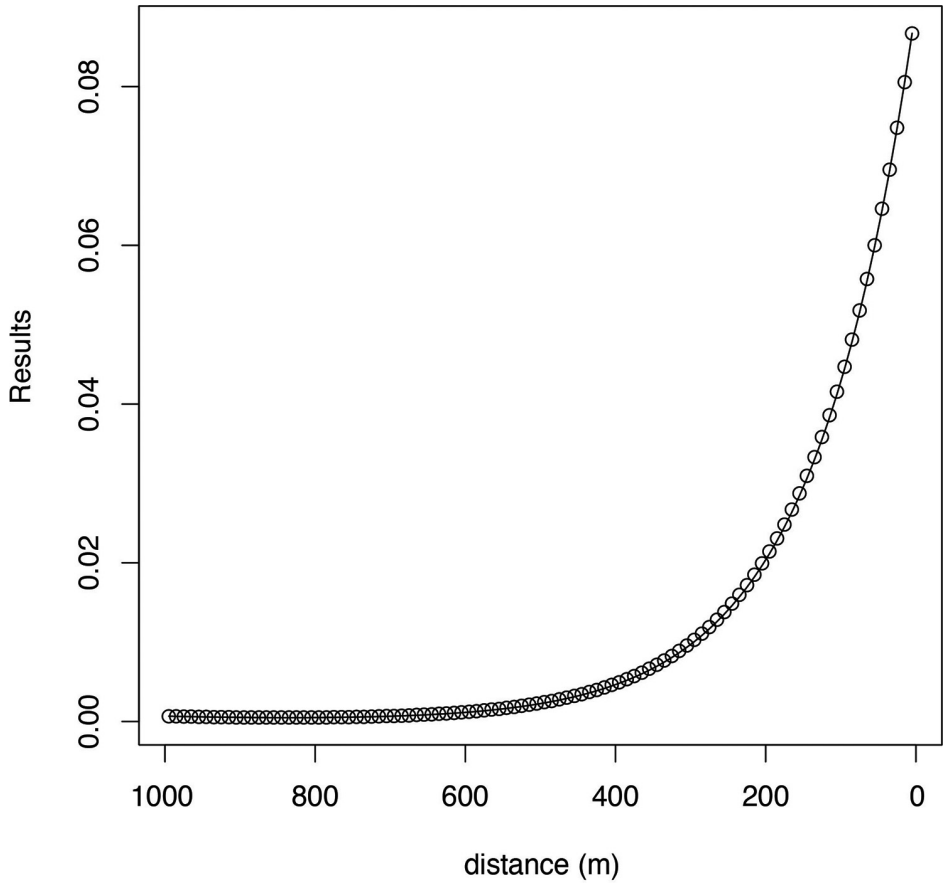


Fig. A1. A model run against a 1D benchmark with analytical solution. $R^2 = 0.99999$. The dots represent model results. The line represents analytical solution of equation $D\frac{\partial^2 C}{\partial x^2} - \vartheta\frac{\partial C}{\partial x} - kC = 0$, where $D = 31.55693$, $\vartheta = 0.1$ and $k = 0.001$. The boundary conditions are $x = 0$, $C = 0.00069$, and $x = 1000$, $C = 0.09$.

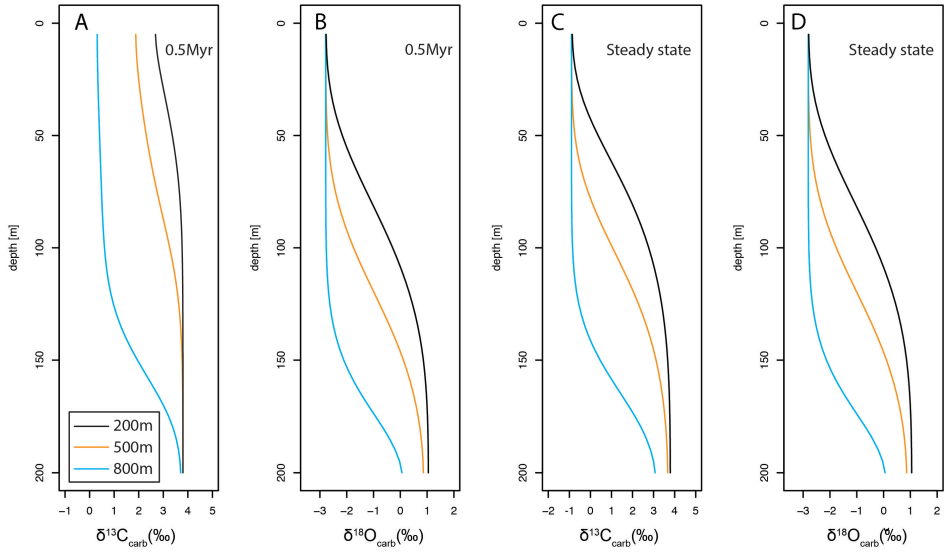


Fig. A2. Stratigraphic trends in $\delta^{13}C_{carb}$ and $\delta^{18}O_{carb}$ values at different vertical slices of the model domain, as analogs for sampling stratigraphic sections across different facies/positions of the same platform. (A-B) model results at 0.5 Myr. (C-D) model results at steady state. The parameters are the same as those in the baseline run.

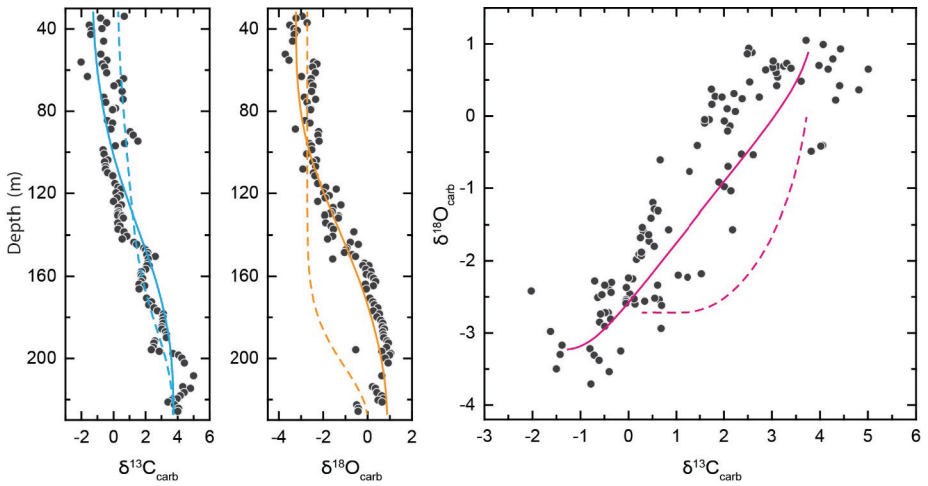


Fig. A3. Model results for two subaerial exposure events for the Great Bahama Bank. The data is from Oehlert and Swart (2014). The dotted lines represent the results of the first subaerial exposure event. The solid lines represent the final results for the combination of the two subaerial exposure events. The hydrological conditions for the first and second subaerial exposure events are the same as fig. A7.B and the baseline run, respectively. $\delta^{13}C_{FW} = -2.5‰$, $\delta^{18}O_{FW} = -3‰$, $DIC_{FW} = 2.3$ mM. The other parameters are the same as the baseline run (tables 1 and 2). The model ran at 0.2 Myr for each subaerial exposure event. The initial conditions for the second subaerial exposure event equal the final results of the first subaerial exposure event. Note that we have not considered the diagenetic processes between subaerial exposure events, and the variations of hydrological conditions during sea level fluctuations because these parameters are largely unknown. The results shown are from the vertical slice at 400 m.

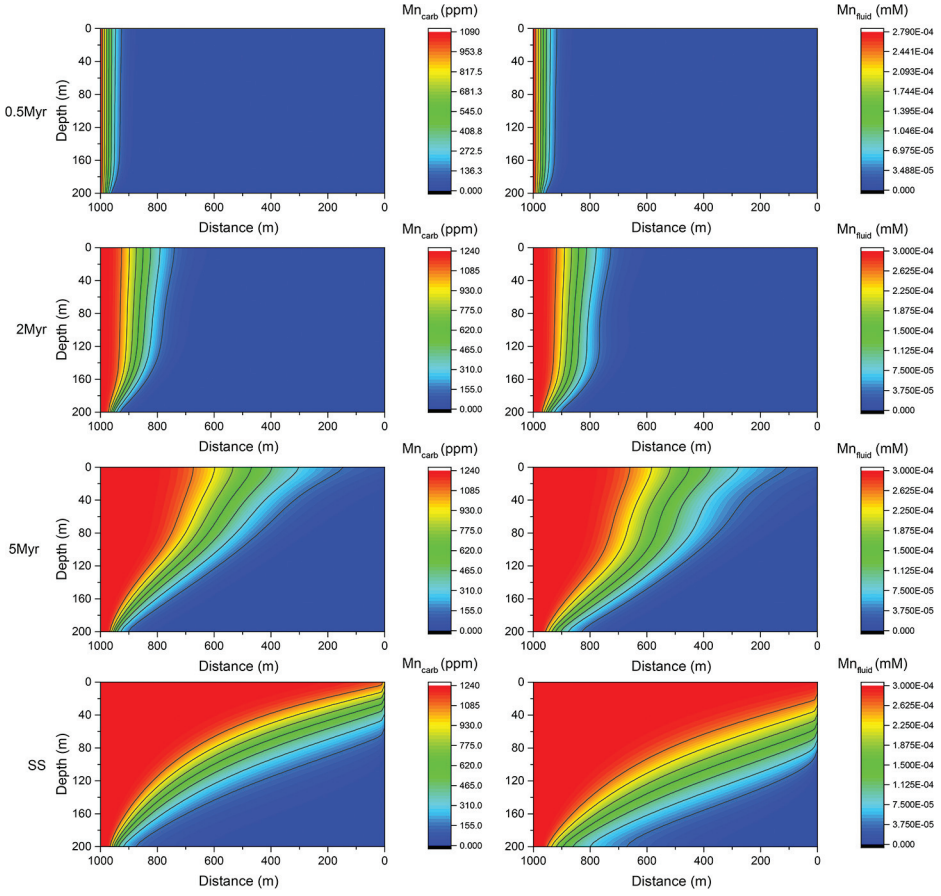


Fig. A4. The time evolution of [Mn] in calcite and fluids of the whole domain for the baseline run. SS represents steady state. See tables 1–3 for the parameters in these runs.

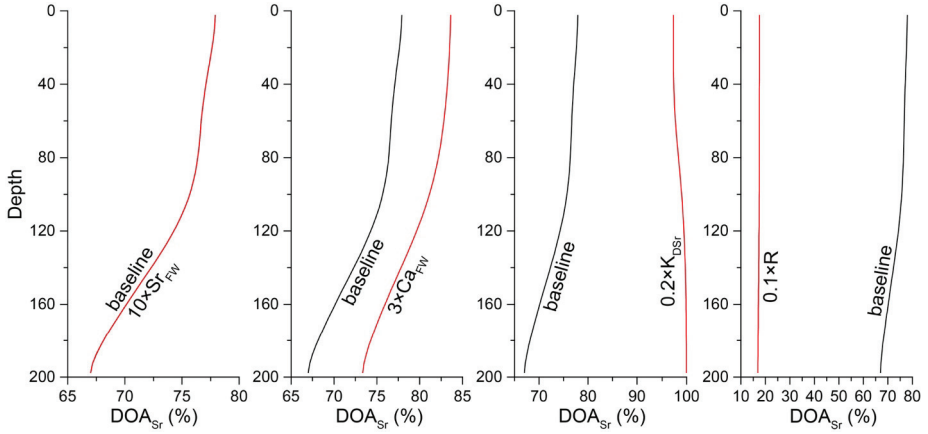


Fig. A5. Degree of alteration for Sr in the stratigraphic profile at 0.2 Myr. There are the same runs as figures 9A, 9C, 9E and 9G. The results presented are from the vertical slices at 500 m from the 2D results.

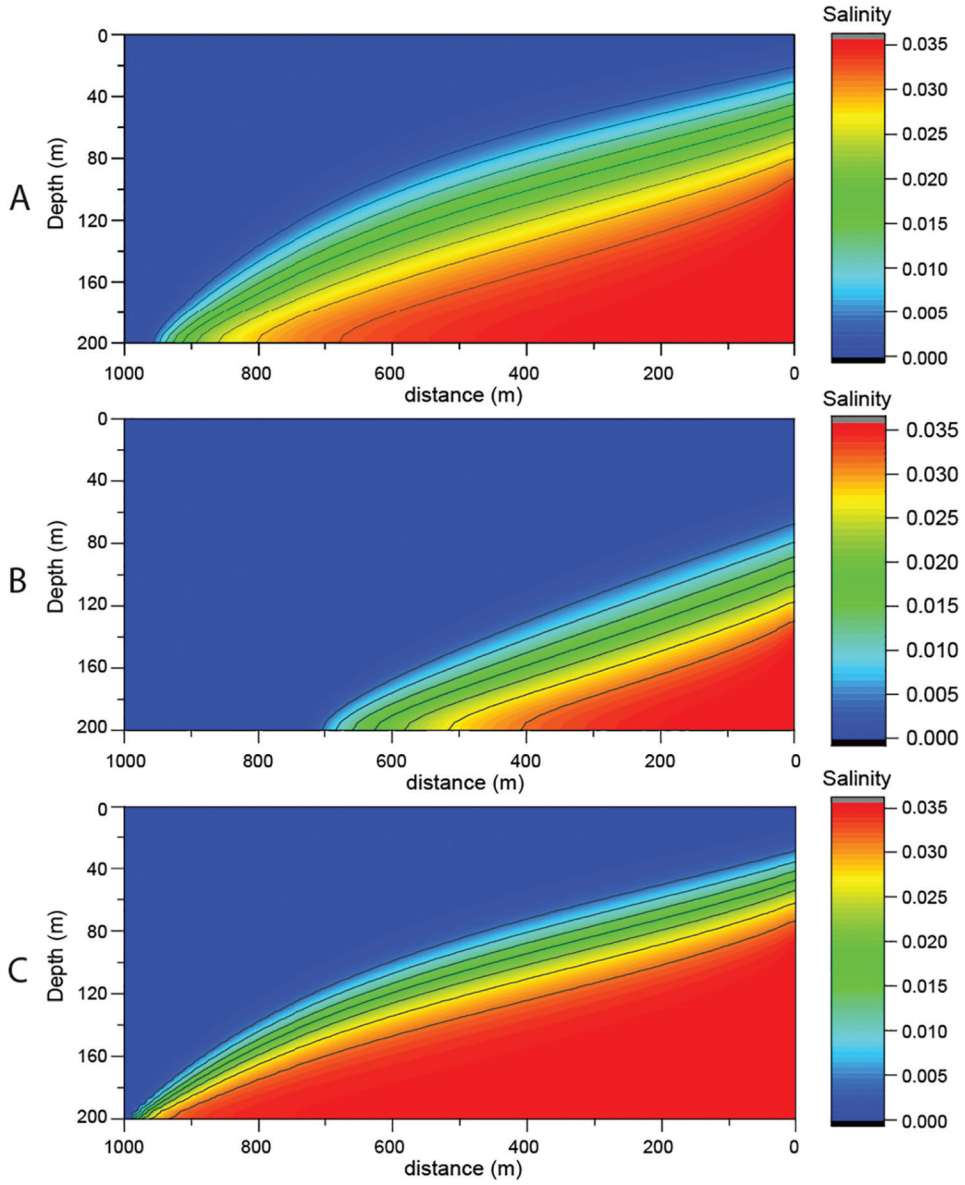


Fig. A6. The influence of the freshwater input rate and the dispersion on the distribution of salinity in the whole domain for (A), the baseline run (B), 2x freshwater discharge rates relative to the baseline run, and (C) 0.3x dispersion relative to the baseline run. These are the same conditions run for model results shown in figure 10.

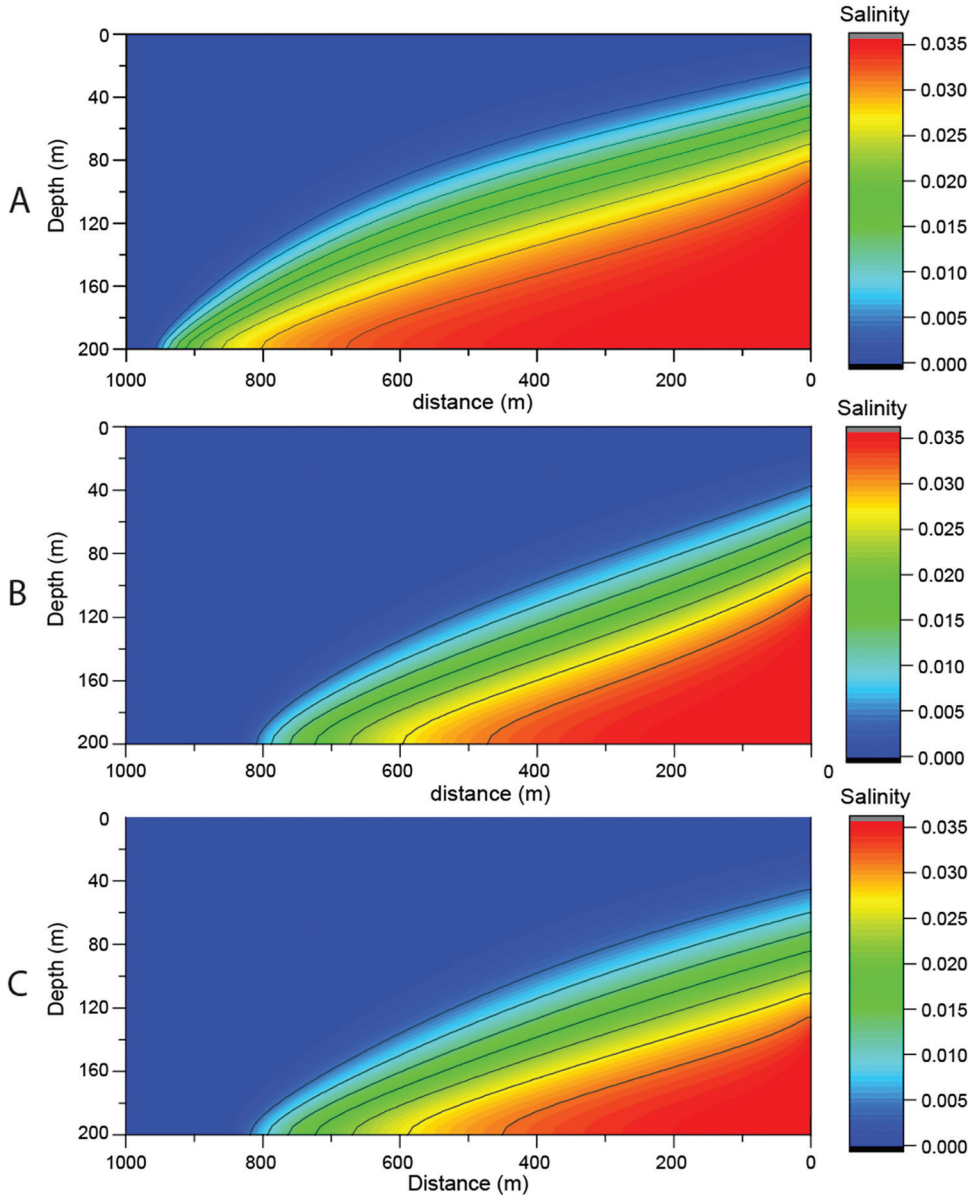


Fig. A7. The influence of horizontal and vertical permeabilities on the distribution of salinity in the whole domain for (A) the baseline run, (B) 0.5 times the horizontal permeability relative to the baseline run, and (C) 0.5 times the vertical permeability relative to the baseline run.

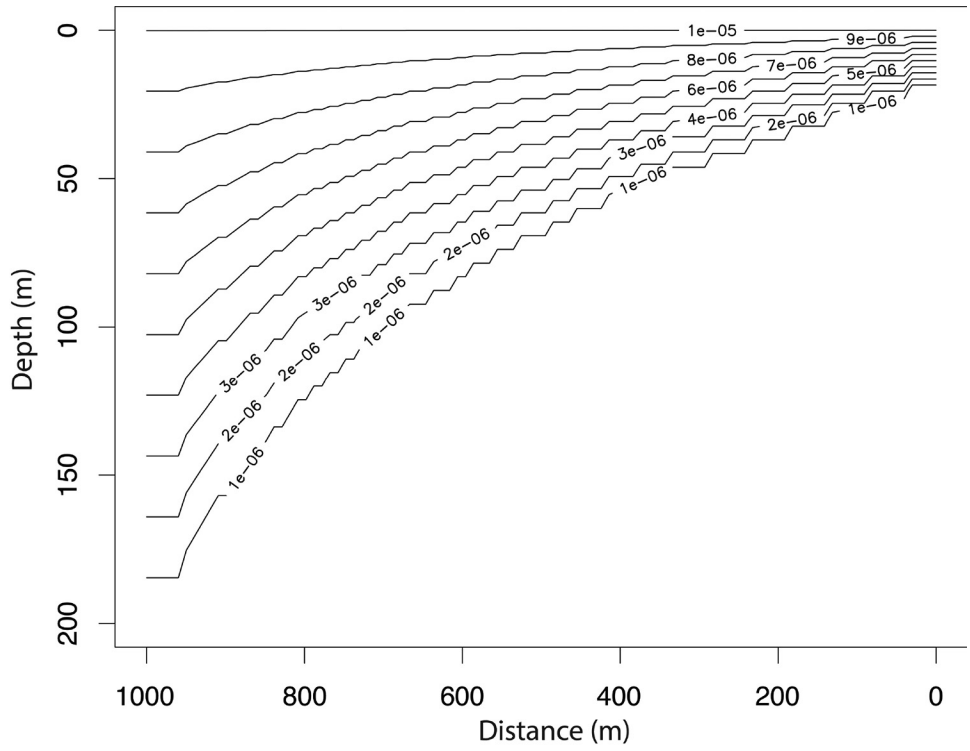


Fig. A8. Recrystallization rate in the model input for the runs with varying recrystallization rate. The recrystallization rate was set as the baseline value at the top of the model domain, but as zero at bottom of the phreatic zone.

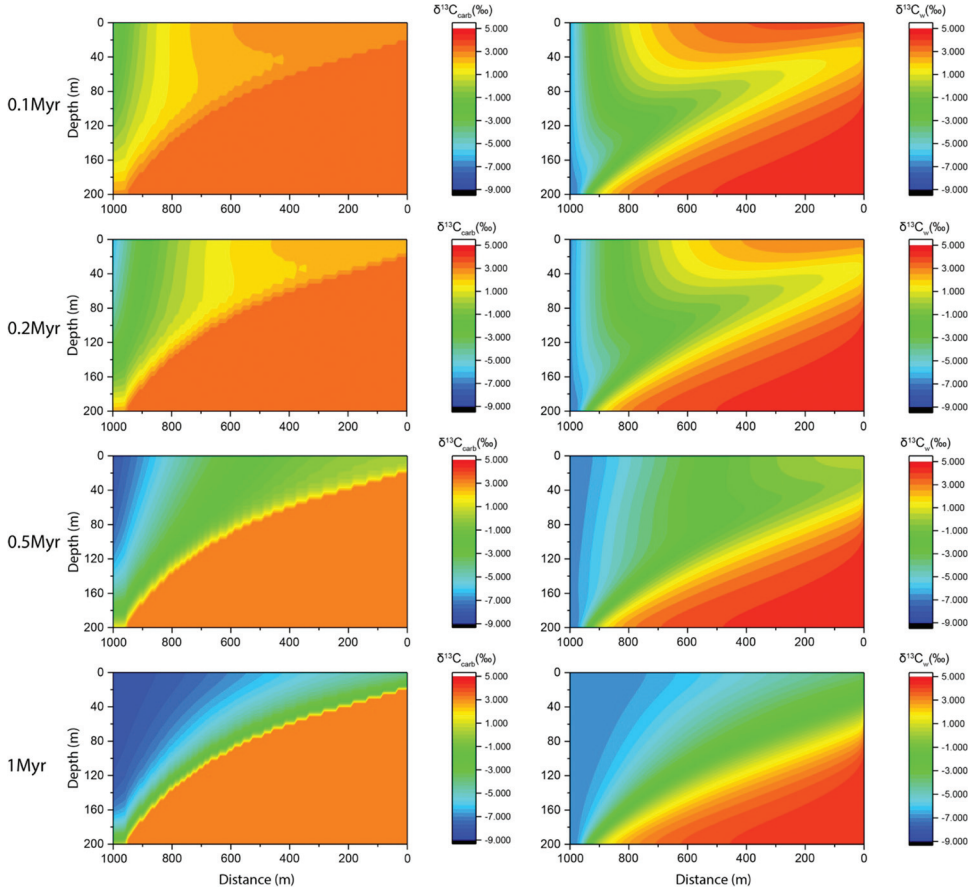


Fig. A9. The temporal evolution of $\delta^{13}C$ values of calcite and fluid in the whole domain for the varying recrystallization rate run. The left panel represents calcite results, while the right panel represents fluid results. The recrystallization rate was set as the baseline value at the top of the model domain, but as zero at bottom of the phreatic zone. The other parameters are the same with the baseline run (tables 1 and 2).

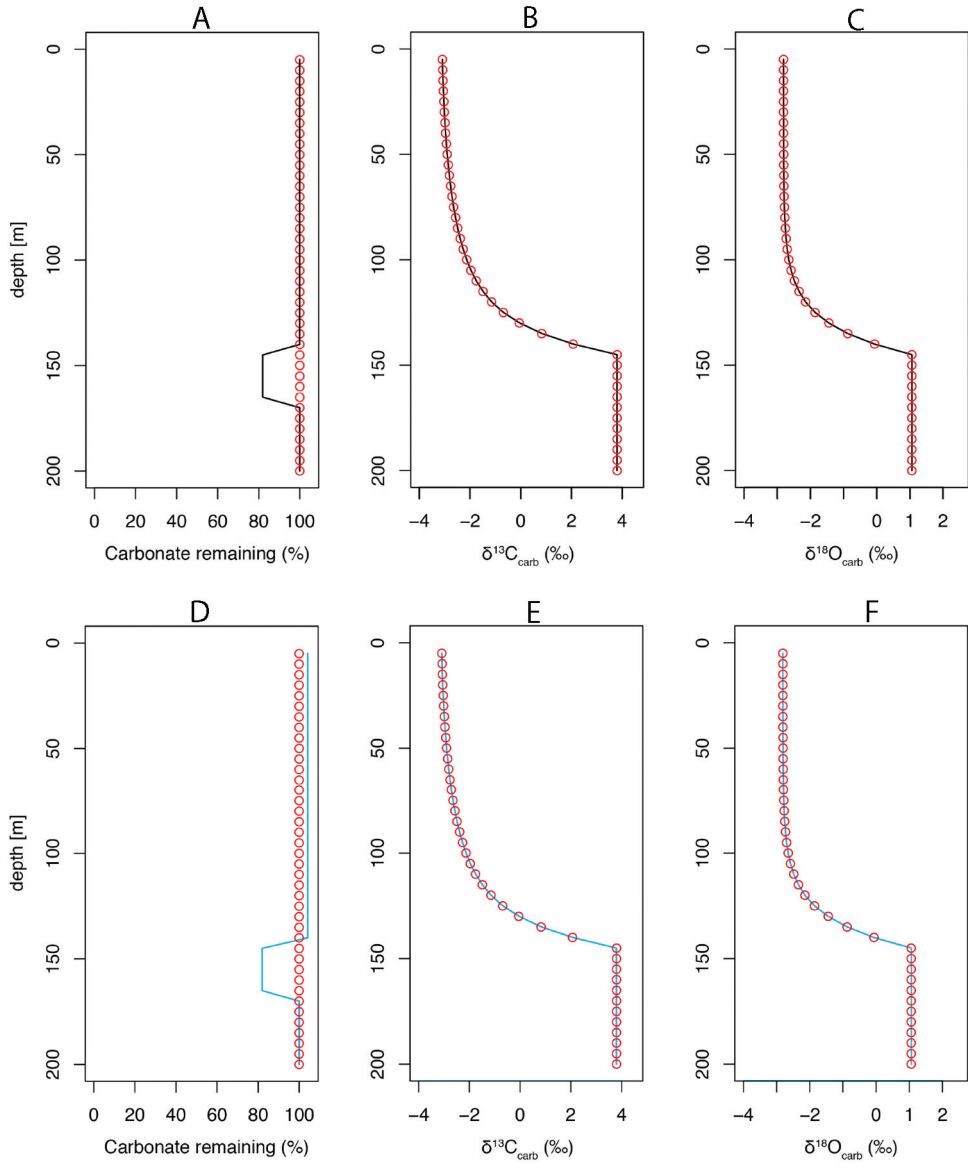


Fig. A10. The influences of net carbonate dissolution in the mixing zone and/or net carbonate precipitation in the phreatic zone. Dots, without net carbonate dissolution or precipitation; lines, with net carbonate dissolution and/or precipitation. (A, B, C) The influences of net carbonate dissolution in the mixing zone. (D, E, F) the influences of net carbonate dissolution in the mixing zone and net carbonate precipitation in the phreatic zone. (A) the percentage of carbonate remained after 1 Myr, with or without net dissolution in the upper part of the mixing zone (with 1% to 20% seawater, Swart and Oehlert, 2018). (B) $\delta^{13}C$ of carbonates after 1 Myr. (C) $\delta^{18}O$ of carbonates after 1 Myr. (D) the percentage of carbonate remained after 1 Myr, with or without net dissolution in the upper part of the mixing zone (with 1% to 20% seawater) and net precipitation in the phreatic zone (Swart and Oehlert, 2018). (E) $\delta^{13}C$ of carbonates after 1 Myr. (F) $\delta^{18}O$ of carbonates after 1 Myr. Other than net carbonate dissolution and/or precipitation, the other model parameters are the same with the run in fig. 11. The results are from the vertical slices at 850 m.

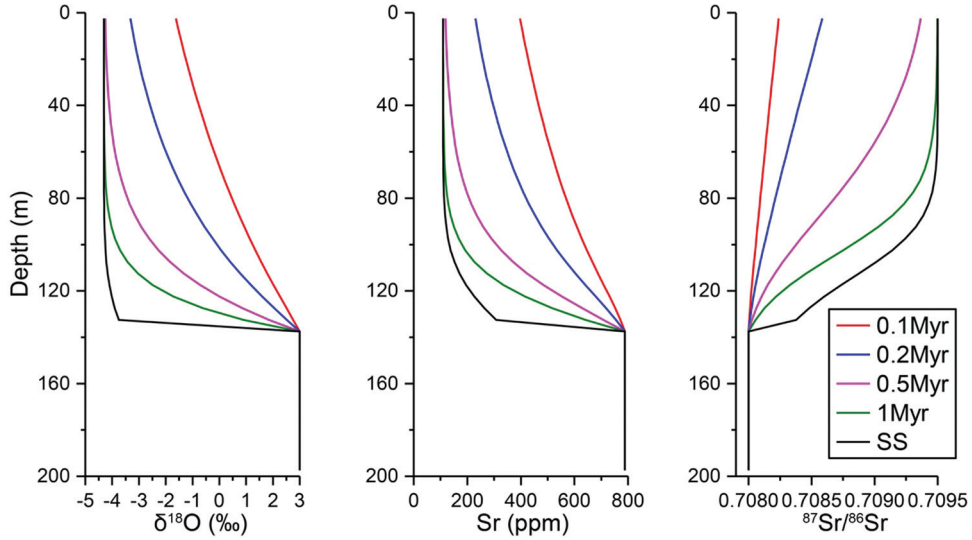


Fig. A11. Modeled time evolutions in the profiles of [Sr], $\delta^{18}O$ values and $^{87}Sr/^{86}Sr$ ratios for carbonates. The results are the vertical slices at 800 m. SS represents the steady-state profile. The recrystallization rate was set as the baseline value at the top of the model domain, but as zero at bottom of the phreatic zone. The other parameters are the same with the baseline run (tables 1 and 2).

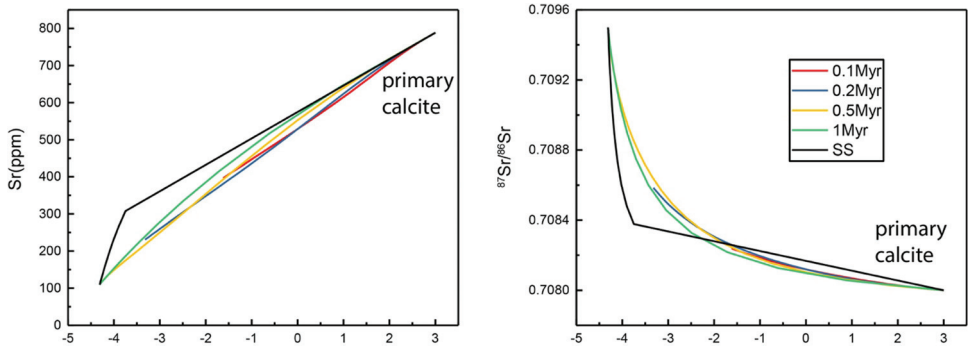


Fig. A12. Modeled relationships between $^{87}Sr/^{86}Sr$ ratios, [Sr] and $\delta^{18}O$ values of a selected vertical slice at different times, for the same model runs presented in fig. A11. The results are from the vertical slices at 800 m. The recrystallization rate was set as the baseline value at the top of the model domain, but as zero at bottom of the phreatic zone. The other parameters are the same as the baseline run (tables 1 and 2). SS represents the steady-state profile.

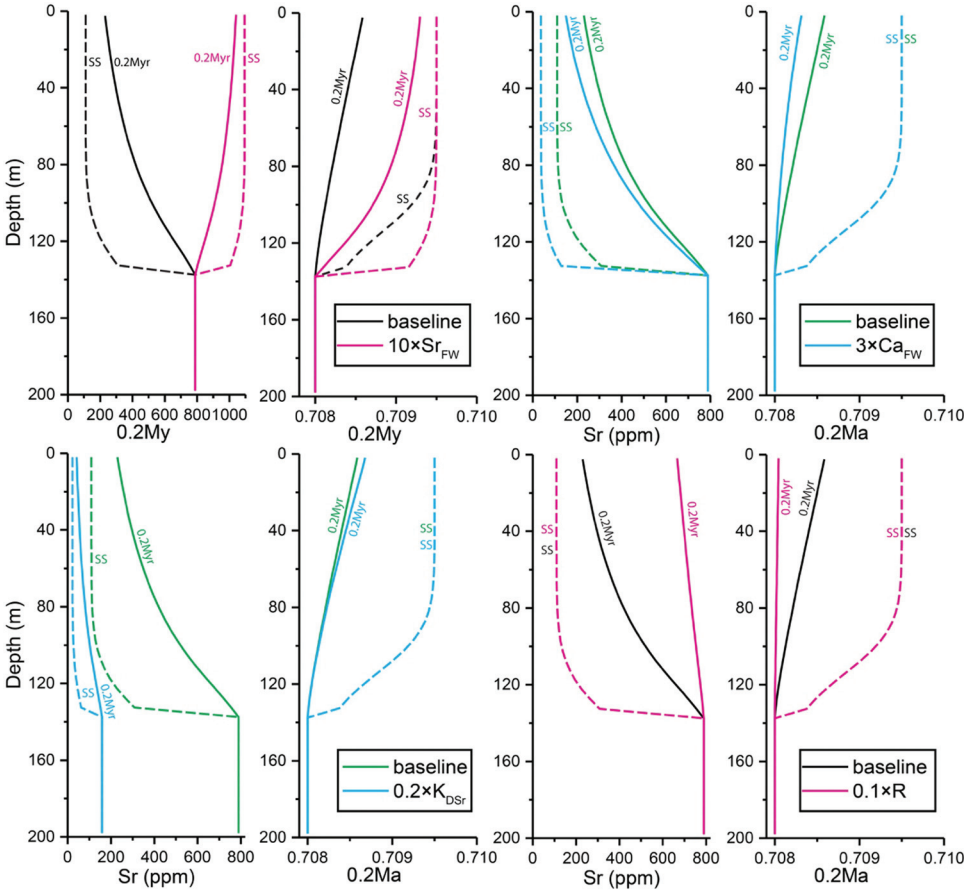


Fig. A13. The influence of non-hydrological factors on the rates for Sr and Sr isotopes in limestone profiles. (A, B) The influence of Sr concentration, with a 10x increase in the Sr concentration of freshwater ($Sr_{FW}$) when compared to the baseline run. (C, D) The influence of Ca concentration, with a 3x increase in the Ca concentration of freshwater ($Ca_{FW}$). (E, F) The influence of the distribution coefficient ($K_{DSr}$) between calcite and water. (G, H) The influence of recrystallization rates. The results are the vertical slices at 800 m. The solid lines represent results at 0.2 Myr, while the dotted lines represent steady-state results. The recrystallization rate was set as the baseline value at the top of the model domain, but as zero at bottom of the phreatic zone. The other parameters are the same as the baseline run (tables 1 and 2).

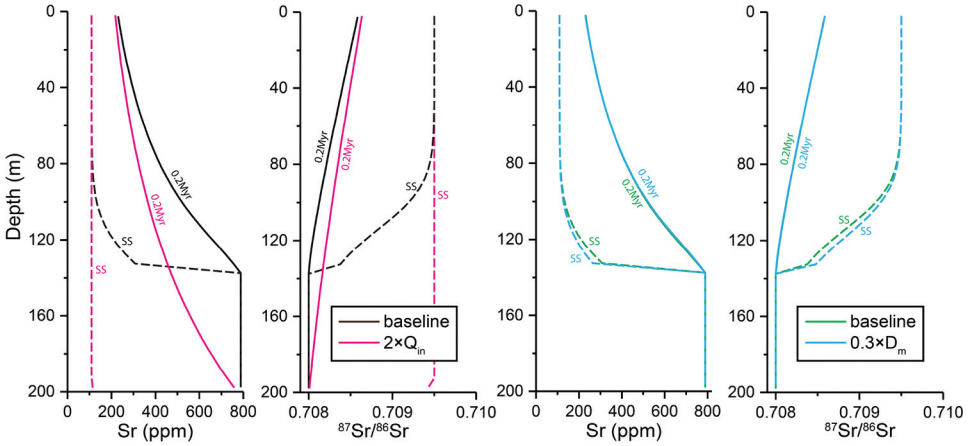


Fig. A14. The influence of hydrological parameters on the rates for Sr and Sr isotopes in limestone profiles. (A, B) The influence of freshwater discharge rates. (C, D) The influence of dispersion. The results are the vertical slices at 500 m.

## REFERENCES


Ahm, A. S. C., Bjerrum, C. J., Blättler, C. L., Swart, P. K., and Higgins, J. A., 2018, Quantifying early marine diagenesis in shallow-water carbonate sediments: Geochimica et Cosmochimica Acta, v. 236, p. 140–159, https://doi.org/10.1016/j.gca.2018.02.042

Allan, J. R., and Matthews, R. K., 1982, Isotope signatures associated with early meteoric diagenesis: Sedimentology, v. 29, n. 6, p. 797–817, https://doi.org/10.1111/j.1365-3091.1982.tb00085.x

Appelo, C. A. J., and Postma, D., 2004, Geochemistry, Groundwater and Pollution: London, England, CRC Press, https://doi.org/10.1201/9781439833544

Avrahamov, N., Sivan, O., Yechieli, Y., and Lazar, B., 2013, Carbon isotope exchange during calcite interaction with brine: Implications for $^{14}C$ dating of hypersaline groundwater: Radiocarbon, v. 55, n. 1, p. 81–101, https://doi.org/10.1017/S0033822200047822

Banner, J. L., 1995, Application of the trace element and isotope geochemistry of strontium to studies of carbonate diagenesis: Sedimentology, v. 42, n. 5, p. 805–824, https://doi.org/10.1111/j.1365-3091.1995.tb00410.x

Banner, J. L., and Hanson, G. N., 1990, Calculation of simultaneous isotopic and trace element variations during water-rock interaction with applications to carbonate diagenesis: Geochimica et Cosmochimica Acta, v. 54, n. 11, p. 3123–3137, https://doi.org/10.1016/0016-7037(90)90128-8

Banner, J. L., and Kaufman, J., 1994, The isotopic record of ocean chemistry and diagenesis preserved in non-luminescent brachiopods from Mississippian carbonate rocks, Illinois and Missouri: GSA Bulletin, v. 106, n. 8, p. 1074–1082, https://doi.org/10.1130/0016-7606(1994)106<1074:TIROOC>2.3.CO;2

Banner, J. L., Hanson, G. N., and Meyers, W. J., 1988, Rare earth element and Nd isotopic variations in regionally extensive dolomites from the Burlington-Keokuk Formation (Mississippian): Implications for REE mobility during carbonate diagenesis: Journal of Sedimentary Research, v. 58, n. 3, p. 415–432, https://doi.org/10.1306/212F8DAA-2B24-11D7-8648000102C1865D

Bear, J., and Verruijt, A., 2012, Modeling groundwater flow and pollution (Vol. 2): Dordrecht, Springer Science & Business Media, 414 p.

Begg, S. H., and Carter, R. R., 1987, Assigning effective values to simulator grid-block parameters for heterogeneous reservoirs: Society of Petroleum Engineers paper, 16754, p. 601–611.

Bowen, G. J., and Revenaugh, J., 2003, Interpolating the isotopic composition of modern meteoric precipitation: Water Resources Research, v. 39, n. 10, https://doi.org/10.1029/2003WR002086

Bristow, T. F., and Kennedy, M. J., 2008, Carbon isotope excursions and the oxidant budget of the Ediacaran atmosphere and ocean: Geology, v. 36, n. 11, p. 863–866, https://doi.org/10.1130/G24968A.1

Budd, D. A., 1988, Petrographic products of fresh water diagenesis in Holocene ooid sands, Schooner Cays, Bahamas: Carbonates and Evaporites, v. 3, p. 143–163, https://doi.org/10.1007/BF03175114

Calver, C. R., 2000, Isotope stratigraphy of the Ediacarian (Neoproterozoic III) of the Adelaide Rift Complex, Australia, and the overprint of water column stratification: Precambrian Research, v. 100, n. 1–3, p. 121–150, https://doi.org/10.1016/S0301-9268(99)00072-8

Caspard, E., Rudkiewicz, J. L., Eberli, G. P., Brosse, E., and Renard, M., 2004, Massive dolomitization of a Messinian reef in the Great Bahama Bank: A numerical modelling evaluation of Kohout geothermal convection: Geofluids, v. 4, n. 1, p. 40–60, https://doi.org/10.1111/j.1468-8123.2004.00071.x

Chester, R., and Jickells, T., 2012, Marine Geochemistry: Chichester, United Kingdom, John Wiley & Sons, 411 p., https://doi.org/10.1002/9781118349083

Clark, I., 2015, Groundwater Geochemistry and Isotopes: Boca Raton, Florida, CRC press, 456 p., https://doi.org/10.1201/b18347

Clayton, R. N., and Degens, E. T., 1959, Use of carbon isotope analyses of carbonates for differentiation of fresh-water and marine sediments: AAPG Bulletin, v. 43, p. 890–897, https://doi.org/10.1306/0BDA5CF6-16BD-11D7-8645000102C1865D

Derry, L. A., 2010, A burial diagenesis origin for the Ediacaran Shuram–Wonoka carbon isotope anomaly: Earth and Planetary Science Letters, v. 294, n. 1–2, p. 152–162, https://doi.org/10.1016/j.epsl.2010.03.022

Dyer, B., Higgins, J. A., and Maloof, A. C., 2017, A probabilistic analysis of meteorically altered $\delta^{13}C$ chemostratigraphy from late Paleozoic ice age carbonate platforms: Geology, v. 45, n. 2, p. 135–138, https://doi.org/10.1130/G38513.1

Fantle, M. S., 2015, Calcium isotopic evidence for rapid recrystallization of bulk marine carbonates and implications for geochemical proxies: Geochimica et Cosmochimica Acta, v. 148, p. 378–401, https://doi.org/10.1016/j.gca.2014.10.005

Fantle, M. S., and DePaolo, D. J., 2006, Sr isotopes and pore fluid chemistry in carbonate sediment of the Ontong Java Plateau: Calcite recrystallization rates and evidence for a rapid rise in seawater Mg over the last 10 million years: Geochimica et Cosmochimica Acta, v. 70, n. 15, p. 3883–3904, https://doi.org/10.1016/j.gca.2006.06.009

——— 2007, Ca isotopes in carbonate sediment and pore fluid from ODP Site 807A: The $Ca^{2+}$(aq)–calcite equilibrium fractionation factor and calcite recrystallization rates in Pleistocene sediments: Geochimica et Cosmochimica Acta, v. 71, n. 10, p. 2524–2546, https://doi.org/10.1016/j.gca.2007.03.006

Fantle, M. S., and Higgins, J., 2014, The effects of diagenesis and dolomitization on Ca and Mg isotopes in marine platform carbonates: Implications for the geochemical cycles of Ca and Mg: Geochimica et Cosmochimica Acta, v. 142, p. 458–481, https://doi.org/10.1016/j.gca.2014.07.025

Fike, D. A., Grotzinger, J. P., Pratt, L. M., and Summons, R. E., 2006, Oxidation of the Ediacaran ocean: Nature, v. 444, 7120, p. 744–747, https://doi.org/10.1038/nature05345

Gross, M. G., 1964, Variations in the $^{18}O/^{16}O$ and $^{13}C/^{12}C$ ratios of diagenetically altered limestones in the Bermuda islands: The Journal of Geology, v. 72, p. 172–193, https://doi.org/10.1086/626975

Hayes, J. M., Strauss, H., and Kaufman, A. J., 1999, The abundance of $^{13}C$ in marine organic matter and isotopic fractionation in the global biogeochemical cycle of carbon during the past 800 Ma: Chemical Geology, v. 161, n. 1, p. 103–125, https://doi.org/10.1016/S0009-2541(99)00083-2

Higgins, J. A., and Schrag, D. P., 2010, Constraining magnesium cycling in marine sediments using magnesium isotopes: Geochimica et Cosmochimica Acta, v. 74, n. 17, p. 5039–5053, https://doi.org/10.1016/j.gca.2010.05.019

——— 2012, Records of Neogene seawater chemistry and diagenesis in deep-sea carbonate sediments and pore fluids: Earth and Planetary Science Letters, v. 357–358, p. 386–396, https://doi.org/10.1016/j.epsl.2012.08.030

Jacobsen, S. B., and Kaufman, A. J., 1999, The Sr, C and O isotopic evolution of Neoproterozoic seawater: Chemical Geology, v. 161, n. 1–3, p. 37–57, https://doi.org/10.1016/S0009-2541(99)00080-7

James, N. P., and Choquette, P. W., 1984, Diagenesis 9—limestones—the meteoric diagenetic environment: Geoscience Canada, v. 11, n. 4, p. 161–194.

Jones, G. D., and Xiao, Y., 2005, Dolomitization, anhydrite cementation, and porosity evolution in a reflux system: Insights from reactive transport models: AAPG Bulletin, v. 89, n. 5, p. 577–601, https://doi.org/10.1306/12010404078

Jones, G. D., Whitaker, F. F., Smart, P. L., and Sanford, W. E., 2004, Numerical analysis of seawater circulation in carbonate platforms: II. The dynamic interaction between geothermal and brine reflux circulation: American Journal of Science, v. 304, n. 3, p. 250–84, https://doi.org/10.2475/ajs.304.3.250

Kaufman, J., 1994, Numerical models of fluid flow in carbonate platforms: Implications for dolomitization: Journal of Sedimentary Research, v. 64, n. 1a, https://doi.org/10.1306/D4267D2F-2B26-11D7-8648000102C1865D

Land, L. S., 1980, The isotopic and trace element geochemistry of dolomites: The state of the art, *in* Zenger, D. H., Dunham, J. B., and Ethington, R. L., editors, Concepts and Models of Dolomitization: SEPM Special Publication, v. 28, p. 87–110, https://doi.org/10.2110/pec.80.28.0087

Land, L. S., and Epstein, S., 1970, Late Pleistocene diagenesis and dolomitization, North Jamaica: Sedimentology, v. 14, n. 3–4, p. 187–200, https://doi.org/10.1111/j.1365-3091.1970.tb00192.x

Langmuir, D., 1997, Aqueous Environmental Geochemistry: Upper Saddle River, New Jersey, Prentice Hall, 600 p.

Lohmann, K. C., 1987, Geochemical patterns of meteoric diagenetic systems and their application to the study of paleokarst, *in* James, N. P., and Choquette, P. W., editors, Paleokarst: Berlin, Springer-Verlag, p. 58–80, https://doi.org/10.1007/978-1-4612-3748-8_3

Maliva, R. G., 1998, Skeletal aragonite neomorphism—quantitative modelling of a two-water diagenetic system: Sedimentary Geology, v. 121, n. 3–4, p. 179–190, https://doi.org/10.1016/S0037-0738(98)00080-3

Marshall, J. D., 1992, Climatic and oceanographic isotopic signals from the carbonate rock record and their preservation: Geological Magazine, v. 129, n. 2, p. 143–160, https://doi.org/10.1017/S0016756800008244

Matthews, R. K., 1968, Carbonate diagenesis: Equilibration of sedimentary mineralogy to the subaerial environment; coral cap of Barbados, West Indies: Journal of Sedimentary Research, v. 38, n. 4, https://doi.org/10.1306/74D71B13-2B21-11D7-8648000102C1865D

McClain, M. E., Swart, P. K., and Vacher, H. L., 1992, The hydrogeochemistry of early meteoric diagenesis in a Holocene deposit of biogenic carbonate: Journal of Sedimentary Petrology, v. 62, n. 6, p. 1008–1022, https://doi.org/10.1306/D4267A37-2B26-11D7-8648000102C1865D

Melim, L. A., Anselmetti, F. S., and Eberli, G. P., 2001, The importance of pore type on permeability of

Neogene carbonates, Great Bahama Bank, *in* Ginsburg, R. N., editor, Subsurface geology of a prograding carbonate platform margin, Great Bahama Bank: Results of the Bahamas Drilling Project: SEPM Special Publication, v. 70, p. 217–238, https://doi.org/10.2110/pec.01.70.0217

Melim, L. A., Westphal, H., Swart, P. K., Eberli, G. P., and Munnecke, A., 2002, Questioning carbonate diagenetic paradigms: Evidence from the Neogene of the Bahamas: Marine Geology, v. 185, n. 1, p. 27–53, https://doi.org/10.1016/S0025-3227(01)00289-4

Melim, L. A., Swart, P. K., and Eberli, G. P., 2004, Mixing-zone diagenesis in the subsurface of Florida and the Bahamas: Journal of Sedimentary Research, v. 74, n. 6, p. 904–913, https://doi.org/10.1306/042904740904

Metzger, J. G., and Fike, D. A., 2013, Techniques for assessing spatial heterogeneity of carbonate $\delta^{13}C$ values: Implications for craton-wide isotope gradients: Sedimentology, v. 60, n. 6, p. 1405–1431, https://doi.org/10.1111/sed.12033

Meyers, W. J., 1989, Trace element and isotope geochemistry of zoned calcite cements, Lake Valley Formation (Mississippian, New Mexico): Insights from water-rock interaction modeling: Sedimentary Geology, v. 65, p. 3–4, p. 355–370, https://doi.org/10.1016/0037-0738(89)90034-1

Oehlert, A. M., and Swart, P. K., 2014, Interpreting carbonate and organic carbon isotope covariance in the sedimentary record: Nature Communications, v. 5, article n. 4672, https://doi.org/10.1038/ncomms5672

O'Neil, J. R., Clayton, R. N., and Mayeda, T. K., 1969, Oxygen isotope fractionation in divalent metal carbonates: The Journal of Chemical Physics, v. 51, n. 12, p. 5547–5558, https://doi.org/10.1063/1.1671982

Paterson, R. J., Whitaker, F. F., Smart, P. L., Jones, G. D., and Oldham, D., 2008, Controls on early diagenetic overprinting in icehouse carbonates: Insights from modeling hydrological zone residence times using CARB3D+: Journal of Sedimentary Research, v. 78, n. 4, p. 258–281, https://doi.org/10.2110/jsr.2008.029

R development core team, 2006, R: A language and environment for statistical computing: Vienna, Austria, R Foundation for Statistical Computing, v. 61, n. 4, p. 1673–1676.

Rezaei, M., Sanz, E., Raeisi, E., Ayora, C., Vázquez-Suñé, E., and Carrera, J., 2005, Reactive transport modeling of calcite dissolution in the fresh-salt water mixing zone: Journal of Hydrology, v. 311, n. 1, p. 282–298, https://doi.org/10.1016/j.jhydrol.2004.12.017

Sanford, W. E., and Konikow, L. F., 1989, Simulation of calcite dissolution and porosity changes in saltwater mixing zones in coastal aquifers: Water Resources Research, v. 25, n. 4, p. 655–667, https://doi.org/10.1029/WR025i004p00655

Sawaki, Y., Ohno, T., Tahata, M., Komiya, T., Hirata, T., Maruyama, S., Windley, B. F., Han, J., Shu, D., and Li, Y., 2010, The Ediacaran radiogenic Sr isotope excursion in the Doushantuo Formation in the three Gorges area, South China: Precambrian Research, v. 176, n. 1–4, p. 46–64, https://doi.org/10.1016/j.precamres.2009.10.006

Soetaert, K., Petzoldt, T., and Setzer, R. W., 2010, Solving differential equations in R: Package deSolve: Journal of Statistical Software, v. 33, n. 9, p. 1–25, https://doi.org/10.18637/jss.v033.i09

Steinen, R. P., and Matthews, R. K., 1973, Phreatic vs. vadose diagenesis: Stratigraphy and mineralogy of a cored borehole on Barbados, W.I.: Journal of Sedimentary Research, v. 43, n. 4, p. 1012–1020, https://doi.org/10.1306/74D728D8-2B21-11D7-8648000102C1865D

Swanson-Hysell, N. L., Rose, C. V., Calmet, C. C., Halverson, G. P., Hurtgen, M. T., and Maloof, A. C., 2010, Cryogenian glaciation and the onset of carbon-isotope decoupling: Science, v. 328, n. 5978, p. 608–611, https://doi.org/10.1126/science.1184508

Swart, P. K., 2000, The oxygen isotopic composition of interstitial waters: Evidence for fluid flow and recrystallization in the margin of Great Bahama Bank, *in* Swart, P. K., Eberil, G. P., and Malone, M., editors, Proceedings of ODP Science Results: Scientific Results, v. 166, p. 91–98, https://doi.org/10.2973/odp.proc.sr.166.130.2000

——— 2008, Global synchronous changes in the carbon isotopic composition of carbonate sediments unrelated to changes in the global carbon cycle: Proceedings of the National Academy of Sciences of the United States of America, v. 105, n. 37, p. 13,741–13,745, https://doi.org/10.1073/pnas.0802841105

——— 2015, The geochemistry of carbonate diagenesis: The past, present and future: Sedimentology, v. 62, n. 5, p. 1233–1304, https://doi.org/10.1111/sed.12205

Swart, P. K., and Kennedy, M. J., 2012, Does the global stratigraphic reproducibility of $\delta^{13}C$ in Neoproterozoic carbonates require a marine origin? A Pliocene–Pleistocene comparison: Geology, v. 40, n. 1, p. 87–90, https://doi.org/10.1130/G32538.1

Swart, P. K., and Oehlert, A. M., 2018, Revised interpretations of stable C and O patterns in carbonate rocks resulting from meteoric diagenesis: Sedimentary Geology, v. 364, p. 14–23, https://doi.org/10.1016/j.sedgeo.2017.12.005

Steefel, C. I., and Maher, K., 2009, Fluid-rock interaction: A reactive transport approach: Reviews in Mineralogy and Geochemistry, v. 70, n. 1, p. 485–532, https://doi.org/10.2138/rmg.2009.70.11

Vahrenkamp, V. C., and Swart, P. K., 1990, New distribution coefficient for the incorporation of strontium into dolomite and its implications for the formation of ancient dolomites: Geology, v. 18, n. 5, p. 387–391, https://doi.org/10.1130/0091-7613(1990)018<0387:NDCFTI>2.3.CO;2

Voss, C. I., and, Provost, A.M., 2010, SUTRA: a model for saturated–unsaturated variable-density groundwater flow with solute or energy transport: U.S. Geological Survey Water-Resources Investigations, U.S. Geological Survey, Reston, Virginia, 260 p.

Wang, Y., and Cerling, T. E., 1994, A model of fossil tooth and bone diagenesis: Implications for paleodiet reconstruction from stable isotopes: Palaeogeography, Palaeoclimatology, Palaeoecology, v. 107, n. 3–4, p. 281–289, https://doi.org/10.1016/0031-0182(94)90100-7

Whitaker, F. F., and Smart, P. L., 1990, Active circulation of saline ground waters in carbonate platforms:

Evidence from the Great Bahama Bank: Geology, v. 18, n. 3, p. 200–203, https://doi.org/10.1130/0091-7613(1990)018<0200:ACOSGW>2.3.CO;2

——— 1997, Groundwater circulation and geochemistry of a karstified bank–marginal fracture system, South Andros Island, Bahamas: Journal of Hydrology, v. 197, n. 1–4, p. 293–315, https://doi.org/10.1016/S0022-1694(96)03274-X

——— 2007, Geochemistry of meteoric diagenesis in carbonate islands of the northern Bahamas: 1. Evidence from field studies: Hydrological Processes, v. 21, n. 7, p. 949–966, https://doi.org/10.1002/hyp.6532

Zhao, M., and Zheng, Y. F., 2014, Marine carbonate records of terrigenous input into Paleotethyan seawater: Geochemical constraints from Carboniferous limestones: Geochimica et Cosmochimica Acta, v. 141, p. 508–531, https://doi.org/10.1016/j.gca.2014.07.001

——— 2017, A geochemical framework for retrieving the linked depositional and diagenetic histories of marine carbonates: Earth and Planetary Science Letters, v. 460, p. 213–221, https://doi.org/10.1016/j.epsl.2016.11.033